Review of progress in the materials development of Re, Os, and Ir-based double perovskite oxides

Jie Chen,[1,2,*] Hai L. Feng,[3] Kazunari Yamaura [1,4]

1. Research Center for Materials Nanoarchitectonics (MANA), National Institute for Materials Science, Namiki 1-1, Tsukuba, Ibaraki 305-0044, Japan
2. Materials Science and Engineering Program, Mechanical Engineering, University of Texas at Austin, Austin, Texas 78712, USA
3. Beijing National Laboratory for Condensed Matter Physics and Institute of Physics, Chinese Academy of Sciences, Beijing 100190, P. R. China
4. Graduate School of Chemical Sciences and Engineering, Hokkaido University, North 10 West 8, Kita-ku, Sapporo, Hokkaido 060-0810, Japan

* To whom correspondence should be addressed.
Present address: Laboratory for Materials and Structures, Institute of Innovative Research, Tokyo Institute of Technology, Yokohama, Kanagawa 226-8503, Japan
Email: is.jiechen@gmail.com

Abstract
This review explores the experimental advancements in the materials development of three 5d transition metal-based double perovskite oxides (Re, Os, and Ir), which have been predominantly achieved under high pressure. Perovskite oxides have ignited substantial interest due to their remarkable attributes encompassing ferroelectricity, piezoelectricity, catalysis, high-temperature superconductivity, giant magnetoresistance, ionic conduction, and negative thermal expansion. The seminal discovery of copper oxide-based high-temperature superconductors in 1986 marked a pivotal milestone in this field. The creation of double perovskite oxides, accomplished by introducing distinct elements into the B site of a perovskite-type structure, opens new avenues for scientific exploration and practical applications. Notably, double perovskite oxides featuring the 5d element at the B site could unveil significant relativistic effects and distinctive characteristics absent in conventional perovskite-type oxides. A high-pressure and high-temperature synthesis method has played a pivotal role in these studies. The ongoing exploration for new 5d double perovskites and a comprehensive understanding of the physical properties within this compound family remain at the forefront. The flexibility inherent in the double perovskite structure enables variations in A-site and B-site elements, along with the incorporation of 5d elements (Re, Os, and Ir), resulting in a diverse range of physical properties. This review systematically compiles synthesized compounds of Re, Os, and Ir-based double perovskite oxides. It also elucidates the impact of crystal structure on several intriguing properties and explores potential applications across various technological and scientific domains. By providing a comprehensive panorama, it aims to enhance comprehension and drive advancements in oxide materials research.

Keywords
Double perovskite oxides; 5d-element; Advanced oxide materials; Perovskite-type structures; High-pressure synthesis

1. Introduction

The exploration of perovskite-type oxides has captivated the materials research community, garnering significant attention for their potential in developing diverse industrial and engineering materials. These materials exhibit remarkable properties, including ferroelectricity, piezoelectricity, catalysis, high-temperature superconductivity, giant magnetoresistance, ionic conduction, and negative thermal expansion, fueling a profound interest in further research and applications. A particularly noteworthy breakthrough was the discovery in 1986 of high-temperature superconductors based on cuprates, propelling research progress to new heights and igniting a wave of enthusiasm in this field. Within the realm of perovskite-type structures, the investigation of double perovskite oxides has emerged as a captivating focus, offering unique opportunities for scientific exploration and practical applications [1-6]. By introducing two elements at the B site in a 1:1 ratio (herein defined by the general formula as $A_2BB'O_6$), these compounds unveil distinct characteristics, inspiring comprehensive studies on their synthesis and properties.

The investigation of double perovskite oxides has unveiled intriguing structural arrangements, with many adopting layered, columnar, or rock-salt configurations. The presence of 5d electrons at the B' site has sparked significant interest due to the profound influence of relativistic effects, leading to the manifestation of unique properties. This review delves into the captivating world of rock-salt type double perovskite oxides, with a focus on those involving 5d-electron configurations at the B' site. These materials exhibit extraordinary properties not commonly found in traditional perovskite-type oxides, motivating us to compile a comprehensive list of successfully synthesized compounds. Notably, among these studies, the high-pressure and high-temperature method has proven to be a useful approach for the synthesis of these compounds. The core focus of this paper lies in exploring the captivating properties of 5d-electron double perovskite oxides and their potential implications for various technological fields from an experimental perspective. With attention to detail, our aim is to present a comprehensive overview of the advances made in experimental synthesis and investigation of these compounds, shedding light on their fascinating properties and promising applications.

To illustrate the electronic structure evolution from 3d to 5d, we performed calculations on a cubic perovskite lattice (space group: *Pm*-3*m*) without structural distortion, specifically focusing on group 8 elements. Notably, all atoms occupy special positions in the crystallographic sense, resulting in an absence of local distortion, ensuring no impact on the electronic state from lattice distortion. The electronic states of the 3d oxide $BaFeO_3$ exhibit a high density of states at the Fermi energy and a relatively narrow d-bandwidth, while the 4d and 5d oxides show progressively wider bandwidths and smaller densities of states (Fig. 1.1). Our nonmagnetic calculations consider the contribution of spin-orbit coupling (SOC). However, for a more comprehensive comparison with actual properties, further investigation involving U (on-site repulsion) and hopping integrals is necessary. It is evident that larger spatial overhang of electron orbitals in elements with larger atomic numbers leads to more pronounced relativistic effects. The results demonstrate that U tends to be smaller in 5d elements compared to 3d elements, exemplifying the significance of these effects. Based on this theoretical calculation, it is evident that 5d oxides distinguish themselves from their 3d and 4d analogues in terms of the nature of the 5d element. This observation motivates further experimental exploration and study of 5d-related oxide compounds.

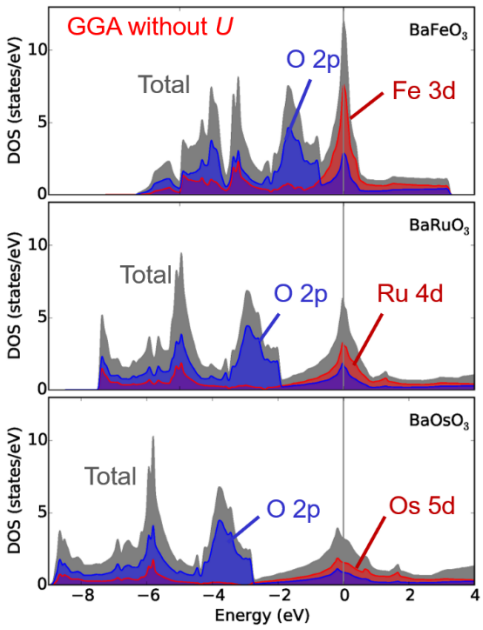

Fig. 1.1: Electronic states of the cubic perovskite (*Pm*-3*m*) in $BaFeO_3$ [7], $BaRuO_3$ [8], and $BaOsO_3$ [9] calculated using density functional theory with generalized gradient approximation [10]. The consideration of spin-orbit coupling was incorporated in the non-magnetic calculations.

The Review comprises four main sections. The Introduction offers an overview of the topic and sets the stage for subsequent sections. The second section delves into the material synthesis and crystal structure of $A_2BB'O_6$ double perovskite oxides, laying the groundwork for further exploration. The main section is divided into two subsections, focusing on the properties of 3d-5d double perovskite oxides, with a particular emphasis on Os- and Re-based compounds. In subsection 3.1, we investigate the high-temperature ferrimagnetism of $A_2FeB'O_6$ and $A_2CrB'O_6$ (*B*' = Os, Re), along with the magnetic properties of A_2BOsO_6 with different A-site elements (*A* = Ca, Sr, Ba; *B* = Fe, Co, Ni). Additionally, we explore the properties of Os-based double perovskite oxides with *A* = Pb and oxides containing Re or Os with nonmagnetic elements in the B site. Section 3.2 outlines properties associated with various B-site elements (nonmagnetic elements, Co, Ni) and various A-site combinations (*A* = Sr, Ba; *B* = Ca, Mg, Zn, Cu, Ni), focusing on Ir-based double perovskite oxides. Finally, we discuss the results presented here, including our own work, and provide future prospects for 5d-based double perovskite oxides.

Through this comprehensive review, we aim to contribute to a broader understanding of the remarkable properties and potential applications of 5d-based double perovskite oxides, while stimulating further research and innovation in the domain of advanced oxide materials.

2. Material synthesis and crystal structures of $A_2BB'O_6$

The early synthesis of 5d double perovskite oxides can be traced back to the 1960s [11,12]. However, intensive experimental efforts to synthesize and characterize double-perovskite compounds composed mainly of the 5d element have been made over the past two decades. In general, conventional solid-state reaction methods are used to synthesize double perovskite oxides. This solid-state reaction, performed at ambient pressure, is sufficient to synthesize many members

of this compound family. Molten salt-mediated synthetic methods have also been employed in the preparation of this compound family [13]. However, for the synthesis of double perovskite compounds, in which the 5d element is the major component, thermal treatment under high-pressure conditions of the gigapascal magnitude has often proven to be effective. Double-perovskite compounds synthesized under high pressure have been reported in the range up to 8 GPa. Various types of high-pressure apparatus have been utilized to achieve pressure conditions in this range, including belt (Fig. 2.1), cubic multi-anvil, and Kawai (also known as Walker) types. For reference, Table 2.1 lists the double perovskite oxides $A_2BB'O_6$ synthesized under high pressure that have been reported.

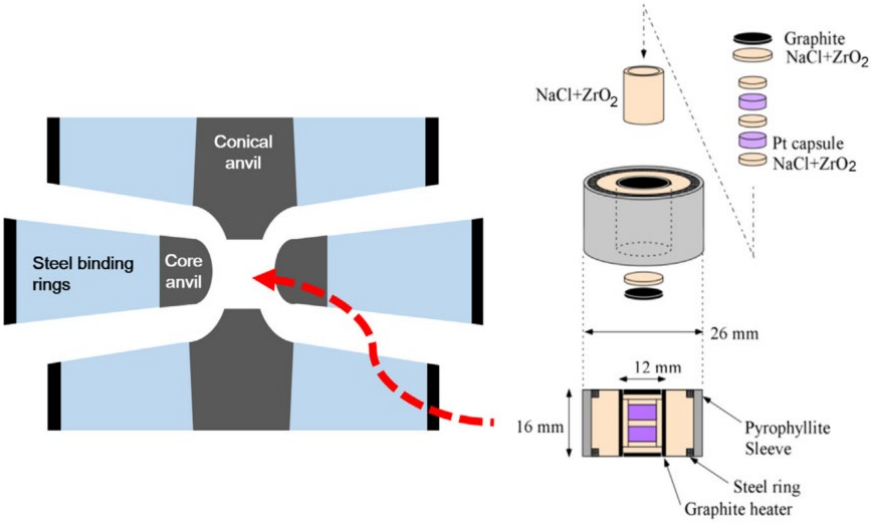

Fig. 2.1: Assembled views of a belt-type high-pressure apparatus and sample cell, located at the National Institute for Materials Science (NIMS) in Japan, used for synthesizing a series of compositionally or structurally new osmate double perovskites [14-18]. Please note that the view may not accurately represent the relative sizes and shapes of the apparatus, as the anvils are somewhat exaggerated [19]. Reprinted from J. Solid State Chem., vol 236, Yamaura, K., Short Review of High-Pressure Crystal Growth and Magnetic and Electrical Properties of Solid-State Osmium Oxides, 45-54, Copyright (2016), with permission from Elsevier.

The formula for double perovskite oxides is generally denoted as $A_2BB'O_6$. However, compounds with the formula $A_2BB'O_6$ can adopt a variety of structures, including rock salt-ordered double perovskite, polytype perovskite, columnar or layered-ordered double perovskite, ilmenite, $LiNbO_3$-type, and corundum-related structures [20-24]. It is worth noting that although not classified as a double perovskite, there are also compounds known as antisite disordered perovskites that have a chemical composition of $A_2BB'O_6$. For instance, Ca_2MnOsO_6 crystallizes into an orthorhombic perovskite structure (*Pnma*) with lattice constants a = 5.50666 Å, b = 7.60562 Å, and c = 5.39317 Å. In this structure, both Mn and Os occupy the same B sites without an ordered arrangement. In this review, the double perovskite structure refers specifically to the rock-salt ordering at the B site and the disorder at the A site. It is important to mention that perovskites with ordered A-site elements also constitute a large family of compounds. Further details on these can be found in other review articles [25,26].

Double perovskite oxides with the most symmetric cubic structure and space group *Fm*-3*m* can be regarded as the ideal crystal structure representing this category. Similar to simple

perovskite-type structures, the tolerance factor of cubic double perovskites is approximately 1 (t = 1). This tolerance factor quantifies the bond mismatch between the A-O and B-O bonds and can be calculated using the formula $t = (r_A + r_O)/(\sqrt{2}(r_B + r_O))$. The cubic double perovskite has approximately twice the unit cell edge size compared to cubic perovskite ABO_3. When the tolerance factor is smaller than 1 (t < 1), an octahedral tilt is expected to occur, resulting in a less symmetric structure. P. M. Woodward and C. J. Howard provided a comprehensive description and review of the symmetry lowering of the crystal structure of the ordered double perovskite $A_2BB'O_6$ [27,28]. Based on group theory analysis by Howard *et al.*, a total of 12 different spatial groups were identified for the ordered double perovskite [28]. For the 5d double perovskite oxides discussed in this paper, at least five of the predicted space groups have been experimentally identified: *Fm*-3*m* (No. 225, $a^0a^0a^0$), *R*-3 (No. 148, $a^-a^-a^-$), *I*4/*m* (No. 87, $a^0a^0c^-$), *P*2$_1$/*n* (No. 14, $a^+b^-b^-$) and *I*2/*m* (No. 12, $a^0b^-b^-$) (Fig. 2.2). This means that the double perovskite-type structure with cubic symmetry decreases in symmetry to rhombohedral (*R*-3), tetragonal (*I*4/*m*), and possibly monoclinic (*P*2$_1$/*n* and *I*2/*m*). Conversely, when the tolerance factor is greater than 1 (t > 1), a hexagonal perovskite-type structure is formed. For example, Ba_2FeOsO_6 (t = 1.0491), Ba_2CoOsO_6 (t = 1.0416), and Ba_2NiOsO_6 (t = 1.0461) crystallize into 6L-type perovskite structures (No. 164, *P*-3*m*1) [10,11,19]. However, it is important to note that these poly-type perovskite oxides do not fall into the category of salt-ordered double perovskites discussed in this paper, and thus will not be further discussed here. Additionally, it should be noted that the lattice and structural parameters discussed in this review are determined through X-ray diffraction (XRD) or neutron diffraction (ND) measurements.

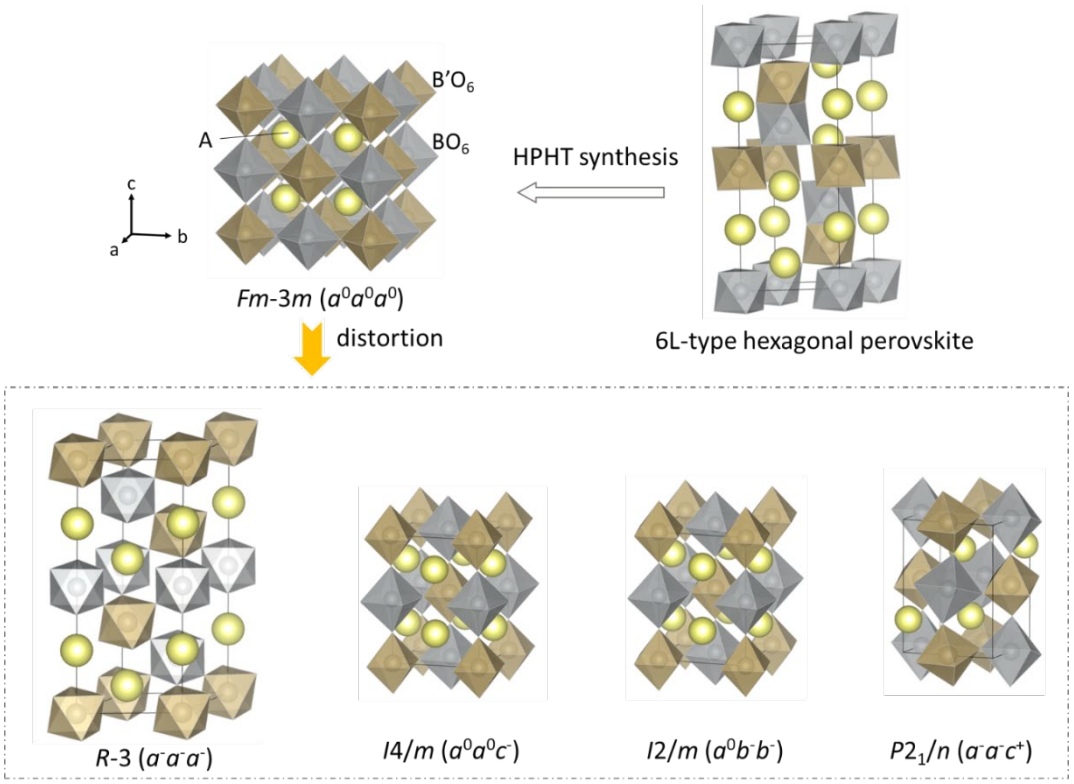

Fig. 2.2: Schematic of the most common five B-site ordered double perovskite structure and 6L-type perovskite structure of $A_2BB'O_6$; the tilted system described using Glazer's notation is shown in parentheses. HPHT denotes high-pressure and high-temperature.

High-pressure and high-temperature techniques have often been shown to be effective in stabilizing perovskites and related structures [29]. In the case of double perovskites, it is possible to create a salt-ordered double perovskite phase even with a tolerance factor greater than 1 ($t > 1$). For instance, Ba_2NiOsO_6 synthesized under 6 GPa pressure exhibits a cubic double-perovskite structure [16], in contrast to the hexagonal phase formed under ambient pressure. This difference may be attributed to the *A*-O bonds being more compressible than the *B*-O bonds under pressure. Consequently, the tolerance factor approaches 1 under the stress environment. On the other hand, the rock salt-ordered phase obtained under pressure lacks the face-sharing octahedra present in the hexagonal phase. The redistribution of BO_6 octahedra under pressure leads to a rock-salt ordered double perovskite composed solely of corner-sharing octahedra. This structural arrangement effectively reduces electrostatic repulsion, as observed in Pauling's third law [30].

The high-pressure and high-temperature method is also useful in incorporating Mn^{2+} and Pb^{2+} ions into the A site of the double perovskite structure. For example, Mn_2BReO_6 (*B* = Li, Co, Ni, Mn, Fe) compounds have been synthesized by using the high-pressure and high-temperature method, all of which have monoclinic perovskite-type structures ($P2_1/n$) [31-37]. This is attributed to the relatively small tolerance factor. On the other hand, the double perovskite Pb_2BOsO_6 (B = Co, Ni, Zn) possesses a monoclinic perovskite-type structure despite having a tolerance factor larger than 1 [18,38,39]. This structural distortion is attributed to the hybridization of the lone pair electrons on Pb with the surrounding oxygen ions. Thus, while the tolerance factor serves as a useful guideline for predicting the structural distortion of perovskites, it is important to recognize the contribution of other factors as well.

In addition to the lone pair electrons of the A-site ions, the competing covalent nature of the *A*-O and *B*-O bonds may influence the symmetry of the perovskite-type structure. The presence of more ionic *A*-O bonds can lead to the *B*/*B*'-O bonds becoming more covalent and thus shorter than the bond lengths predicted by the hard-sphere model with tabulated ionic radii. For instance, Ba_2BReO_6 (*B* = Fe, Mn, Co, Ni, Zn) and Ba_2BOsO6 (*B* = Li, Mg, Zn, In, Sc) have tolerance factors greater than 1, but these compounds with rock-salt double-perovskite structures can be synthesized without requiring high pressure [40-43]. On the other hand, the development of magnetic ordering can induce structural distortions. In the case of Pb_2CoOsO_6, the presence of magnetic ordering is accompanied by an abrupt change in the lattice constant [18]. Similarly, in Sr_2CoOsO_6 and Sr_2CoReO_6, a symmetry reduction from tetragonal to monoclinic is observed upon the onset of magnetic ordering [44,45]. Furthermore, spin-lattice interactions can affect the stability of the structure, as evidenced by the contraction of the *c*-lattice constant with increasing temperature in the tetragonal double perovskites Sr_2NiReO_6 and Sr_2NiOsO_6 [45,46].

The synthesis of certain 5d double perovskite compounds often requires the application of oxygen pressure to effectively stabilize the high oxidation states of the 5d elements and prevent the formation of oxygen vacancies. In ambient pressure synthesis, the desired oxygen pressure can be achieved by using pressurized oxygen or through the thermal decomposition of oxygen sources such as PbO_2, Ag_2O, and MnO_2 in a sealed reaction container [46-49]. In high-pressure synthesis, perchlorate salts are commonly used as an in-situ source of oxygen. These salts undergo thermal decomposition to produce chloride salts, thereby providing the necessary oxygen for the synthesis [15,50].

Table 2.1: 5d double perovskite oxides obtained by high-pressure and high-temperature conditions.

Compounds	*P* (GPa)	S. G. [a]	*t* [b]	GII [b]	Refs
$5d^0$					
Mn_2LiReO_6	8	$P2_1/n$	0.8652	0.02871	[31]
$5d^1$					
Mn_2CoReO_6	8	$P2_1/n$	0.8571	0.02701	[32]
Mn_2NiReO_6	8	$P2_1/n$ (150 K)	0.8607	0.02480	[33]
Pb_2CoReO_6	8	R-3	0.9926	0.00005	[51]
$5d^{1-2}$					
Mn_2MnReO_6 [c]	5, 8	$P2_1/n$	0.8778/ 0.8368	0.01718/0.04379	[34,35]
$5d^2$					
Mn_2FeReO_6	5	$P2_1/n$	0.8780	0.01711	[36,37]
Pb_2NiReO_6	6	$I2/m$	0.9968	0.00101	[52]
Ca_3OsO_6	6	$P2_1/n$	0.8695	0.04118	[14]
Ca_2MgOsO_6	6	$P2_1/n$	0.9290	0.00616	[53]
Sr_3OsO_6	6	P-1	0.8881	-	[49]
Sr_2MgOsO_6	6	$I4/m$	0.9824	0.02001	[53]
Ba_2NiOsO_6	6	Fm-3m	1.0461	0.42842	[16]
Ba_2CuOsO_6	6	$I4/m$	1.0479	0.44848	[54]
Pb_2CaOsO_6 [d]	6	$P2_1/n$	-	-	[39]
Pb_2CoOsO_6	6	$P2_1/n$	1.0038	0.01937	[18]
Pb_2NiOsO_6	6	$P2_1/n$	1.0081	0.04611	[38]
Pb_2ZnOsO_6	6	$P2_1/n$	1.0008	0.00087	[39]
$5d^3$					
Ca_2InOsO_6	6	$P2_1/n$	0.9034	0.01326	[55]
Pb_2FeOsO_6	8	Fm-3m	1.0110	0.06712	[56]
Sr_2CuIrO_6	4	$I4/m$	0.9875	0.01441	[57]
Ba_2NiIrO_6	8	Fm-3m	1.0450	0.41754	[58]
$5d^5$					
Lu_2NiIrO_6	6	$P2_1/n$	0.8578	0.03420	[59]

[a] The structures listed in the table were determined at room temperature or according to the literature. Any structures determined at temperatures other than room temperature are indicated in the table.

[b] Tolerance factor (t) and the global instability index (GII) are calculated by SPuDS version 2.21.05.11.

[c] Mixed valent states of $Mn^{2+/3+}$ for the B-site and $Re^{6+/5+}$ for B'-site were suggested in ref. [35]. Tolerance factor and GII before the slash was calculated with $R_0(Mn^{3+})$ and $R_0(Re^{5+})$, while the latter was calculated with $R_0(Mn^{2+})$ and $R_0(Re^{6+})$.

[d] Pb_2CaOsO_6 does not crystallize into a typical double perovskite structure, but rather adopts a highly distorted monoclinic structure ($P2_1/n$) with lattice parameters a = 10.0812(3) Å, b = 5.689(1) Å, c = 11.837(4) Å, and β = 125.32(2)° at 2 K. This distorted structure persists at high temperatures. [39]

3. Properties of 5d-electron (Re, Os, and Ir) double perovskite oxides

3.1. Re- and Os-based double perovskite oxides

The high Curie temperature exhibited by magnetic materials makes them appealing for use in magnetic and spintronic devices. Simple perovskites, however, face challenges in achieving a

high Curie temperature, primarily due to the difficulty in establishing a network of orbital ordering that enables three-dimensional ferromagnetic (FM) coupling. In contrast, a group of double perovskite oxides has been discovered to exhibit ferromagnetism or ferrimagnetism (FIM) with remarkably high Curie temperatures (T_C). The exploration and investigation of high-T_C FM double perovskite oxides can be traced back to the studies of Re-based double perovskite oxides in the 1960s [1,2,52]. This early research sparked further interest in exploring other high-T_C FM double perovskite oxides, particularly those based on molybdenum and tungsten. The discovery of half-metallic properties in Sr_2FeMoO_6 in 1998, along with its relatively high T_C (410-450 K), has served as a catalyst for exploring these double perovskite materials in the context of their potential applications in spintronics [60]. Extending to osmate double perovskite oxides, Sr_2CrOsO_6, reported in 2007, stands out with the highest known T_C of 725 K among FIM double perovskite compounds. The discovery of these double perovskite oxides has laid the foundation for new high-T_C FIM materials and has stimulated the understanding of the physics underlying high-T_C magnetism.

It should be noted that the double perovskite oxide Sr_3OsO_6 has recently been reported to exhibit a FM transition above 1000 K in its thin film form fabricated on the $SrTiO_3$ substrate [61]. However, the corresponding bulk materials of Sr_3OsO_6 do not exhibit FM features [49]. This suggests that there may be a contribution from the interface between the film and the substrate, influencing the magnetic behavior.

There is typically no specific temperature criterion for defining a high T_C for ferrimagnetic materials. Nevertheless, it is commonly accepted to classify high-T_C FIM materials as those demonstrating a net magnetic moment above room temperature. In some reports on double perovskites, materials exhibiting spontaneous magnetization are referred to as FM, distinguishing them from antiferromagnetic (AFM) materials, which do not possess spontaneous magnetization. However, in this review, we emphasize the importance of clearly distinguishing between ferrimagnetism (FIM) and ferromagnetic (FM) based on spin alignment. Specifically, we use the term FIM to describe the antiparallel spin alignment between the B and B' sites in double perovskites, where the presence of different transition metal elements at these sites results in a non-zero net spin. In this section, our discussion focuses on FIM Re- and Os-based double perovskites that exhibit a net magnetic moment above room temperature.

Among the reported Re and Os-based double perovskite oxides, it is commonly observed that compounds with Cr or Fe occupying the B site exhibit high-T_C FIM properties, as summarized in Table 3.1. The presence of high-T_C ferrimagnetism in $A_2BB'O_6$ (B = Cr, Fe; B' = Re, Os) double perovskite compounds can be attributed to the specific electronic configurations of Cr^{3+} ($3d^3$) and Fe^{3+} ($3d^5$). The partially filled orbitals of Cr^{3+} and Fe^{3+} are believed to play significant roles in the strong magnetic interactions observed in these materials. It is noteworthy that despite exhibiting high T_C ferrimagnetism, the double perovskite compounds listed in the table also demonstrate a diverse range of electron transport properties.

Table 3.1: Comparison of the structural parameters and physical properties of double perovskite $A_2BB'O_6$ (B = Cr or Fe, B' = Re or Os) with high-T_C ferrimagnetism.

Re-based compounds	**Ca_2CrReO_6**	**Sr_2CrReO_6**	**Ca_2FeReO_6**	**Sr_2FeReO_6**	**Ba_2FeReO_6**	**Mn_2FeReO_6**	**Pb_2FeReO_6**
S.G.	$P2_1/n$	$I4/m$	$P2_1/n$	$I4/m$	Fm-$3m$	$P2_1/n$	$I4/m$
Bond length of B-O (Å)	1.966 × 2 1.973 × 2	1.956 × 4 1.956 × 2	2.025 × 2 2.025 × 2	1.985 × 4 2.004 × 2	2.10291 × 6	1.929 × 2 1.962 × 2	1.98 × 4 1.96 × 2

	1.956 × 2		2.012 × 2			2.060 × 2	
Bond length of B'-O (Å)	1.969 × 2 1.972 × 2 1.976 × 2	1.953 × 4 1.949 × 2	1.959 × 2 1.954 × 2 1.940 × 2	1.961 × 4 1.946 × 2	1.92874 × 6	2.036 × 2 2.018 × 2 1.982 × 2	1.99 × 4 2.01 × 2
Bond angle of B-O-B' (deg.)	154.3 153.1 155.01	179.7 180	151.73 152.24 150.68	170.22 180	180	140.9 139.8 139.7	178.6 180
Tolerance factor (t) [a]	0.9498	1.0043	0.9414	0.9954	1.0552	0.8780	1.0169
GII	0.00176	0.03352	0.00302	0.00539	0.53261	0.01711	0.10371
Electron transport	Insulator	Metal [62,63] Semiconductor [13]	Semiconductor [64,65] Metal-insulator transition [62,63]	Metal [63] Semiconductor [13]	Metal [64] Semiconductor [13]	Insulator	Semiconductor
T_C (K)	360	635	525	400	315	520	420
M_s (μ_B/ formula-it)	0.8	0.86	3	3	3.04	5.0	2.4
Ref.	[63]	[13,62,63]	[62-65]	[63,66]	[64,67,68]	[36,37]	[69]
Os-based compounds	**Ca_2CrOsO_6**	**Sr_2CrOsO_6**	**Ca_2FeOsO_6**				
S.G.	$P2_1/n$	R-3 (RT)	$P2_1/n$				
Bond length of B-O (Å)	1.971 × 2 1.970 × 2 1.972 × 2	1.952 × 6 (500 K)	1.976 × 2 2.020 × 2 2.019 × 2				
Bond length of B'-O (Å)	1.959 × 2 1.962 × 2 1.943 × 2	1.958 × 6 (500 K)	1.986 × 2 1.936 × 2 1.946 × 2				
Bond angle of B-O-B' (deg.)	153.4 153.1 154.20	176.5	151.5 154.0 151.7				
Tolerance factor (t)[a]	0.9443	0.9985	0.9359				
Electron transport	Insulator	Insulator	Insulator				
M_s (μ_B/ formula-nit)	0.2	0.22	~1.5				
T_C, T_N (K)	490	725	320				
Ref.	[70]	[70]	[15,71]				

[a] The tolerance factor (t) and the global instability index (GII) can be calculated using SPuDS version 2.21.05.11.

3.1.1 High temperature ferrimagnetism of $A_2FeB'O_6$ (B' = Re, Os)

Among Re or Os-based double perovskite oxides, the majority exhibit insulating behavior. However, the electronic properties of A_2FeReO_6 (A = Ca, Sr, Ba) distinguish them from other members, ranging from insulating to metallic. Ca_2FeReO_6 has been reported to undergo a metal-insulator transition at 150 K [54,55], while Sr_2FeReO_6 and Ba_2FeReO_6 exhibit metallic behavior [63-65]. Experimental studies and theoretical simulations suggest that Sr_2FeReO_6 and Ba_2FeReO_6 possess half-metallicity, where the conduction electrons are spin-polarized at the Fermi level [68,72-74]. The half-metallic FM or FIM nature of these materials has attracted significant interest due to their potential applications in spintronics, such as high tunnel magnetoresistance. However, the electron transport properties of A_2FeReO_6 (A = Ca, Sr, Ba) reported in different studies are not entirely consistent, as shown in Table 3.1. Resistivity measurements in polycrystalline samples can be influenced by factors such as grain boundary concentration and anti-site disorder, which may contribute to variations in the data. The synthesis method used to prepare these compounds can play

a crucial role in minimizing grain boundary effects and anti-site disordering [13,75].

The FIM half metals, Sr_2FeReO_6 and Ba_2FeReO_6, have attracted significant interest in the field of spintronics due to their similarities to Sr_2FeMoO_6 [60]. The half-metallic and FIM ground states observed in Sr_2FeReO_6 and Ba_2FeReO_6 can be described using a double-exchange-like model similar to that in Sr_2FeMoO_6 [76]. The electronic band crossing the Fermi level in Sr_2FeReO_6 and Ba_2FeReO_6 consists of hybridized orbitals involving Fe (t_{2g} orbital of 3d), O (2p orbitals), and Re (t_{2g} orbitals of 5d) [77]. This hybridization enables the sharing of conduction electrons between Fe and Re ions, leading to mixed-valent states of Fe^{2+}/Fe^{3+} and Re^{6+}/Re^{5+}. The coexistence of Fe^{2+}/Fe^{3+} and Re^{6+}/Re^{5+} has been investigated through Mössbauer and X-ray absorption spectroscopic studies [77-79].

While Re-based and Mo-based double perovskites share certain similarities in their charge configuration and some physical properties, there are also significant differences between the two. Within the framework of a simple ionic model, the distortion of bond angles away from the ideal 180° in double perovskite compounds results in a reduction of effective d-electron hopping or a decrease in the hybridization between the d orbitals of the transition metal ions and the p orbitals of oxygen. In the case of monoclinic Ca_2FeReO_6, the bond angle of *B*-O-*B*' exhibits severe distortion compared to cubic Ba_2FeReO_6 or tetragonal Sr_2FeReO_6. The insulating ground state of Ca_2FeReO_6 seems to be explained by the reduction of effective d-electron hopping between Fe and Re. Interestingly, Ca_2FeMoO_6 also exhibits a comparable distorted bond angle of *B*-O-*B*' to Ca_2FeReO_6. However, unlike Ca_2FeReO_6, Ca_2FeMoO_6 maintains a metallic behavior similar to Sr_2FeMoO_6 [80]. Therefore, solely attributing the insulating nature of Ca_2FeReO_6 to the bond-angle distortion becomes challenging.

Furthermore, the observed elevated T_C in Ca_2FeReO_6 cannot be adequately explained by this mechanism. The experimental observation of Ca_2FeReO_6 having the highest T_C among A_2FeReO_6 (A = Ca, Sr, Ba) double perovskites contradicts the expected outcome, as the reduction of hybridization resulting from the bond-angle distortion would typically lead to a lower T_C. The angle of Fe-O-Re deviates from 180° disturbs the interaction between the t_{2g} orbitals of Fe and Re, known as pdd-π coupling. Instead, it facilitates the pdd-σ coupling through the e_g orbitals of Fe and Re, which has been proposed as the underlying mechanism for the observed increase in ferromagnetic coupling in Ca_2FeReO_6 [74,81].

Band structure calculations have indicated that the insulating state of Ca_2FeReO_6 can be accurately described by incorporating an appropriate on-site Coulomb repulsion term [82]. This discovery suggests that Ca_2FeReO_6 exhibits strong correlation effects, which sets it apart from its electronic analog compounds, Ba_2FeReO_6 and Sr_2FeReO_6. The observed metal-insulator transition in Ca_2FeReO_6 is believed to be associated with a potential orbital transition, which could involve the presence of two competing spin-orbital ordered states [83].

Mn_2FeReO_6 and Pb_2FeReO_6 are two examples of high-T_C FIM double perovskite compounds, where the A-sites are not occupied by alkaline earth ions. The stabilization of the double perovskite forms of Mn_2FeReO_6 and Pb_2FeReO_6 requires high-pressure conditions. By introducing Mn^{2+} at the A-site, a group of transition-metal-only double perovskite materials is formed. Within this family, several Re-based double perovskites have been reported, including Mn_2FeReO_6, Mn_2MnReO_6, Mn_2CoReO_6, and Mn_2NiReO_6 [32-37]. However, no osmate double perovskite compound incorporating Mn^{2+} at the A-site has been identified thus far.

The introduction of Mn^{2+} into the 3d-5d double perovskite leads to more complex magnetic

and electronic properties. In Mn_2FeReO_6, three spin-ordering regimes have been determined from neutron diffraction at different temperatures. At 300 K, the spin structure of Mn_2FeReO_6 is comparable to other FIM double perovskites, with antiparallel ordering between Fe^{3+} and Re^{5+} and no measurable moment from Mn. With cooling, AFM order of Mn^{2+} appears, and the competition between exchange interactions of Mn-O-Mn, Fe-O-Re, and Mn-O-Fe/Re leads to magnetic frustration at low temperatures. Due to the large spin of Mn^{2+} ion (S = 5/2), the magnetization in Mn_2FeReO_6 is significantly higher compared to other members of A_2FeReO_6 (A = Ca, Sr, Ba, Pb). The high-T_C and significant positive magnetoresistance make Mn_2FeReO_6 a promising material for spintronic applications.

The insulating behavior observed in Mn_2FeReO_6 aligns with the trend observed in A_2FeReO_6 (A = Ca, Sr, Ba) as the ionic radius of A^{2+} decreases. In this case, the smaller ionic radius of Mn^{2+} compared to Ca^{2+} accentuates the insulating behavior. This correlation suggests that the transition from metal to insulator is influenced by the size of the A-site cation in these double perovskite compounds.

The electronic properties observed in Pb_2FeReO_6 generally follow the trend seen in the A_2FeReO_6 family regarding the relationship between structural distortion and electron transport. As the temperature decreases, the resistivity of Pb_2FeReO_6 slightly increases, indicating a semiconducting behavior [69]. This contrasts with the metallic behavior observed in A_2FeReO_6 (A = Sr, Ba), where the A-site ions are larger than Pb^{2+}. The insulating nature of Ca_2FeReO_6 below its metal-insulator transition temperature (~150 K) has been investigated using photoemission spectroscopy [69,84].

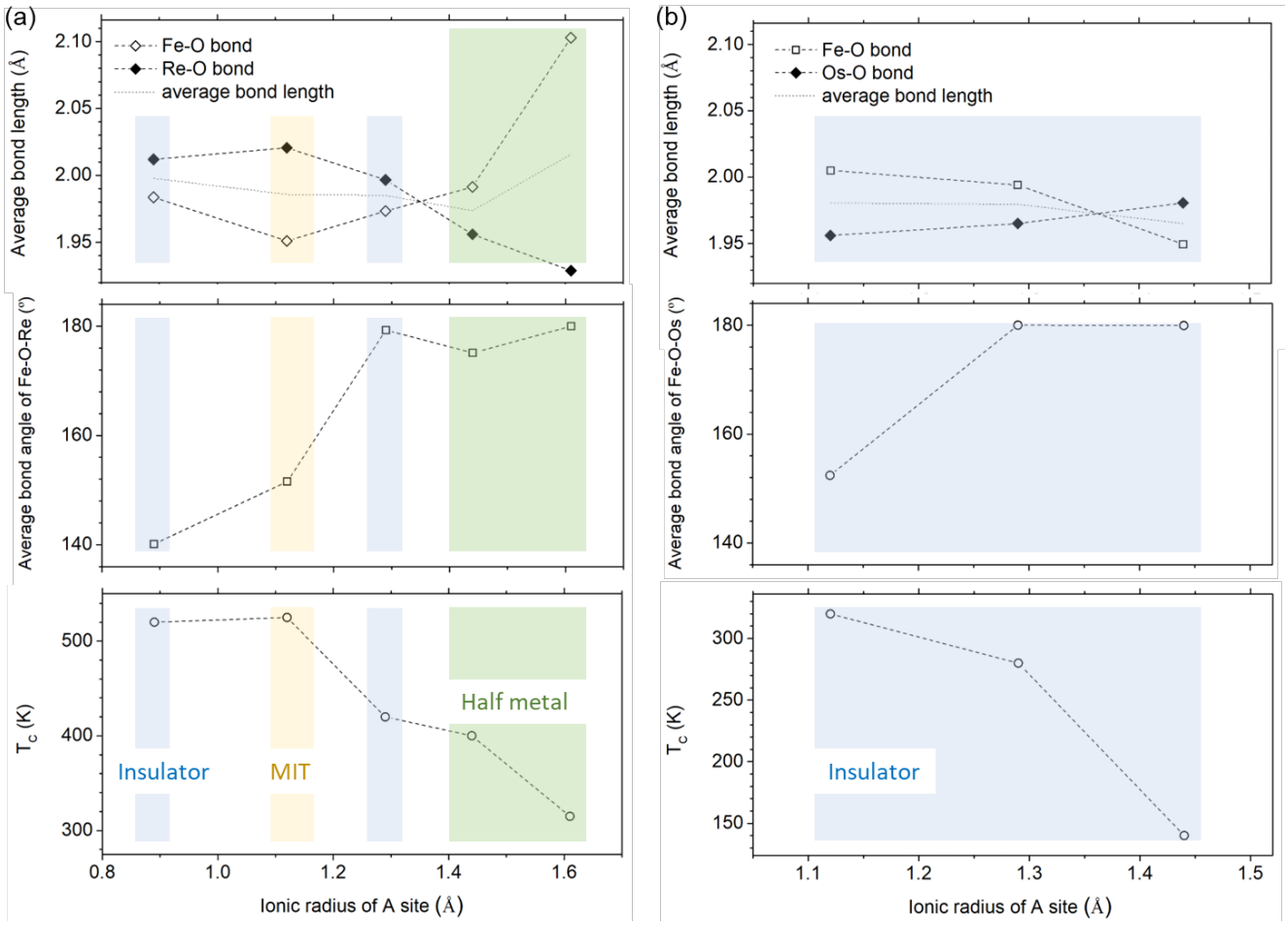

Fig. 3.1: Variations of the T_C, average bond angle, and bond length in two sets of double perovskite compounds. (a) A_2FeReO_6 (A = Ca, Sr, Ba, Mn, Pb) compounds. The data are obtained from the references listed in the accompanying table. The plot allows for a comparison of T_C among the different compounds. (b) A_2FeOsO_6 (A = Ca, Sr, Pb) compounds. The data for Sr_2FeOsO_6 and Pb_2FeOsO_6 are taken from references [56,85], respectively, and are included for comparison with the high-T_C ferrimagnetic compound Ca_2FeOsO_6. It is noted that Sr_2FeOsO_6 exhibits two magnetic phase transitions at 140 K and 67 K, and the magnetic transition temperature of 140 K is depicted in the figure.

The A_2FeReO_6 and A_2FeOsO_6 compounds, sharing the same 3d transition metal but having different 5d transition metals, exhibit variations in their structural characteristics and physical properties. The interplay between the crystal lattice structure, arrangement of transition metal ions, spin states, and electronic states may govern the overall behavior of these high-T_C FIM 5d double perovskite oxides.

To investigate this statement, we compare the structure, magnetic, and transport properties of the two series of 3d-5d double perovskite oxides, as depicted in Fig. 3.1. When larger A-site ions are present, the double perovskite structures undergo a transition from monoclinic to cubic lattice. The inclusion of data for Sr_2FeOsO_6 and Pb_2FeOsO_6 in Fig. 3.1, alongside Ca_2FeOsO_6, provides insights into the evolution within the Fe-Os double perovskite family, despite these compounds not falling into the high-T_C FIM category. This structural transition is evident from the changes in the B-O-B' bond angle. Interestingly, the bond lengths of B-O and B'-O exhibit distinct evolutions with respect to the ionic radii of A-site cations in A_2FeReO_6 and A_2FeOsO_6, despite the similar ionic radii

of Re^{5+} and Os^{5+}.

In A_2FeReO_6, the Fe-O bond length generally increases with larger A-site ions, whereas in A_2FeOsO_6, the Fe-O bond length decreases with larger A-site ions. The trends for Re-O and Os-O bond lengths show opposite behavior accordingly. Although the tolerance factors, calculated from effective ionic radii, are similar for A_2FeReO_6 and A_2FeOsO_6 when the A site is occupied by the same cation, the average bond lengths of B/B'-O exhibit comparable values between these two systems, as indicated by the dashed line in Fig. 3.1.

In terms of the magnetic transition temperature, it consistently decreases as the A-site cation size increases for both A_2FeReO_6 and A_2FeOsO_6. However, despite the similar magnetic trends, the two series demonstrate different transport properties. The A_2FeReO_6 compound family exhibits a wider range of electron transport properties, including insulating behavior, metal-insulator transitions, and half-metallic characteristics. In contrast, all three Fe-Os double perovskites exhibit insulating behavior.

3.1.2 High temperature ferrimagnetism of $A_2CrB'O_6$ (B' = Re, Os)

The d^3 electronic configuration is known to exhibit high magnetic transition temperatures, which is commonly observed in both simple perovskites and double perovskites. For instance, $SrTcO_3$ with a $t_{2g}^3e_g^0$ configuration in its 4d orbital has the highest Neel temperature (T_N) of approximately 1000 K [86]. Another example is $NaOsO_3$, a 5d perovskite with a $5d^3$ electronic configuration, which exhibits a T_N of 410 K [87]. In the case of the $3d^3$-$5d^3$ double perovskite Sr_2CrOsO_6, it demonstrates the highest known T_C among bulk double perovskite oxides, reaching up to 725 K. The mechanisms underlying the observed high-T_C FIM property and its deference from its counterparts, such as Sr_2CrReO_6 and Sr_2CrWO_6, are still being investigated. The specific electronic configurations and the interplay between the 3d and 5d electrons contribute to the unique magnetic properties observed in these systems. Further research is needed to fully understand the factors influencing the high-T_C ferrimagnetism in these materials.

Replacing Os with Re in Sr_2CrReO_6 results in a relatively lower T_C of 635 K, while an even lower T_C of 458 K is found in Sr_2CrWO_6 [88]. This suggests that the AFM exchange interaction originating from the Cr^{3+}-O-Os^{5+} bond is stronger compared to the Cr^{3+}-O-Re^{5+} and Cr^{3+}-O-W^{5+} bonds. The electronic analogues of Sr_2CrOsO_6 and Sr_2CrReO_6, Ca_2CrOsO_6 and Ca_2CrReO_6, crystallize into the monoclinic double perovskite lattice. Similar to Sr_2CrOsO_6 and Sr_2CrReO_6, Ca_2CrOsO_6 exhibits a higher T_C compared to Ca_2CrReO_6. Furthermore, the FIM transition temperature can be influenced by fully or partially substituting Cr^{3+} with other elements [17,89]. These examples highlight the strong correlation between robust high-T_C ferrimagnetism and the AFM exchange interaction originating from the Cr^{3+}-O-Os^{5+} bond. However, the specific reasons for the specialty of d^3 electronic configurations and their impact on the magnetic properties require further studies.

The antiparallel spin arrangement between Cr^{3+} and Os^{5+} in Sr_2CrOsO_6 and Ca_2CrOsO_6 is similar to the spin ordering observed in FIM $A_2FeB'O_6$ compounds. However, there is a distinction in the electronic configuration between Cr^{3+} ($3d^3$) and Fe^{3+} ($3d^5$). While both Cr^{3+} ($3d^3$) and Os ($5d^3$) have three unpaired electrons, the FIM behavior in Sr_2CrOsO_6 and Ca_2CrOsO_6 is influenced by the significant orbital contribution of Os. This non-negligible orbital contribution reduces the magnetic moment on Os, preventing complete compensation between moments of Cr^{3+} and Os^{5+} [70,89].

This observation challenges the simple assumption that SOC is negligible in $5d^3$ systems due to the total orbital angular momentum being zero. It has been found that SOC can be present in $4d^3$ and $5d^3$-based oxides, as they exist in an intermediate electronic state between *L-S* and *j-j* coupling schemes [82,83]. The uncompensated magnetic moments on Cr^{3+} and Os^{5+} contribute to the saturation magnetization (M_s) of Sr_2CrOsO_6, which has been determined to be 0.22 μ_B/formula-unit through neutron diffraction measurements [70]. A comparable value of 0.2 μ_B/formula-unit was found for Ca_2CrOsO_6. The neutron diffraction measurements also confirm the non-monotonic temperature dependence of magnetic susceptibility observed in Sr_2CrOsO_6 and exclude the previously proposed canted magnetic structure [90].

It is worth noting that the M_s values for Cr-5d double perovskites are significantly lower compared to those observed in high-T_C FIM Fe-5d counterparts due to the presence of fewer 3d electrons. However, the magnetic transition temperature is significantly improved in Cr-based analogs.

We have highlighted the properties and behavior of double perovskite oxides containing Cr^{3+}, W^{5+}, Re^{5+}, or Os^{5+} ions. These materials are particularly interesting for investigating the impact of 5d band filling on various physical properties, such as high-temperature ferrimagnetism and electric transport. One notable finding is that the T_C for ferrimagnetism significantly increases with increasing bandwidth within the series of Cr-5d double perovskites. Specifically, Sr_2CrOsO_6 exhibits a T_C higher than that of Sr_2CrWO_6 and Sr_2CrReO_6 by more than 200 K. This suggests that a wider bandwidth leads to a substantial enhancement of T_C.

The electronic properties of these materials also demonstrate changes in band filling. While Sr_2CrWO_6 and Sr_2CrReO_6 display half-metallic behavior and are positioned on the metallic side of a spin-polarized metal-insulator transition [91], Sr_2CrOsO_6 is considered to reside at the terminal point of this transition. Despite having low resistivity at room temperature, Sr_2CrOsO_6 does not exhibit metallic characteristics, indicating that it lies on the boundary of the spin-polarized metal-insulator transition [91].

The observed half-metallic behavior in double perovskite oxides containing Cr^{3+} or Fe^{3+} can be attributed to kinetic-energy-driven ferrimagnetism. This arises from the hybridization between the 3d orbital of Cr^{3+} or Fe^{3+} ions and the 5d orbital of W^{5+}, Re^{5+}, or Os^{5+} ions. This hybridization causes shifts in the energy levels of W^{5+}, Re^{5+}, or Os^{5+} ions, resulting in a significant tendency towards half-metallic properties [79,80].

The AFM order between the 3d and 5d ions in these double perovskites is facilitated by spin-polarized conduction electrons, as previously described [92-94]. This mechanism induces a magnetic moment on the W, Re, and Os sites, consistent with experimental observations [95,96].

3.1.3 Evolution of magnetism with different A-site elements in A_2BOsO_6 (*A* = Ca, Sr, Ba; *B* = Fe, Co, Ni)

The 3d-5d double perovskite oxides exhibit unique electronic and magnetic properties compared to those containing only 3d elements. This distinction can be primarily attributed to the distinct characteristics of the 5d orbitals. Over the past two decades, there has been rapid progress in the discovery of new 3d-Os double perovskite compounds, with high-pressure synthesis playing a crucial role in stabilizing some of these materials.

Most of the reported A_2BOsO_6 compounds (where *A* = Ca, Sr, Ba; *B* = 3d transition metal) exhibit insulating behavior, which is unexpected considering the anticipated stronger hybridization

between the extended 5d orbitals and oxygen, which could potentially lead to metallic properties. However, A_2BOsO_6 compounds display intriguing and unexpected magnetic properties, influenced by various factors such as the large spatial extent of the 5d orbitals, crystal-field splitting effects, and the strong SOC present in these compounds.

The magnetic properties of A_2BOsO_6 compounds have been observed to be effectively altered by substituting A-site cations in osmate double perovskites, often accompanied by structural transitions. In this section, we will review the magnetic properties of several compound families within the A_2BOsO_6 (A = Ca, Sr, Ba; B = 3d transition metal) family. The objective is to gain insights into how the structure influences the magnetic properties of these osmate double perovskites.

Ca_2FeOsO_6 is a FIM material with a high Curie temperature of 320 K [15]. In contrast, the isoelectronic compound Sr_2FeOsO_6 exhibits AFM properties [85,97]. Neutron diffraction studies have determined that Sr_2FeOsO_6 exhibits two types of AFM spin structures at low temperatures, denoted as AF1 and AF2 (Fig. 3.2) [98,99]. In both AF1 and AF2 structures, the magnetic moments of Fe and Os are antiparallel to each other within the ab plane, consistent with the proposed FIM structure of Ca_2FeOsO_6 [15]. The main difference between these two AFM spin structures lies in the spin coupling along the c-axis.

Morrow et al. propose that in the AF1 phase, the FIM ab planes are coupled to neighboring planes by a 90° AFM Os-O-O-Os interaction on the face-centered cubic-type Os sublattice [71]. The AF1 phase emerges at 140 K, while the AF2 phase appears at temperatures below 67 K [71,99]. Paul et al. suggest that the change in the dominant AFM spin structure in Sr_2FeOsO_6 is attributed to a modulation of the Fe-Os distance along the c-axis within the tetragonal lattice as the temperature decreases [99]. Morrow et al. propose an alternative explanation for the AF2 magnetic structure, suggesting that a four-bond Fe-O-Os-O-Fe AFM superexchange coupling dominates along the c-axis, leading to antiparallel coupling of Fe spins along these chains [71].

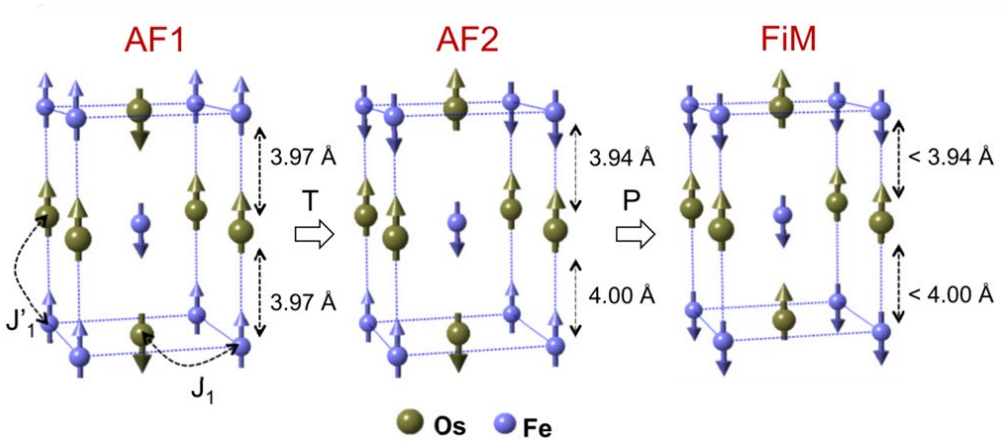

Fig. 3.2: Magnetic structures of antiferromagnetic (AF1, AF2), and ferrimagnetic (FIM) phases observed in Sr_2FeOsO_6 [98]. Reprinted with permission from [Veiga, L. S. I., *et al.*, Phys. Rev. B, 91 (23), 235135, 2015] Copyright (2015) by the American Physical Society.

In comparison to the AF2 phase of Sr_2FeOsO_6, the magnetic moments of Fe and Os in Ca_2FeOsO_6 exhibit complete AFM coupling along the c-axis, as opposed to partial AFM coupling. This difference in behavior is attributed to the distinct crystal structures of Ca_2FeOsO_6 (monoclinic

double perovskite) and Sr_2FeOsO_6 (tetragonal double perovskite), which lead to different magnetic ground states. In the monoclinic lattice of Ca_2FeOsO_6, the Fe-O-Os bond angles along the c-axis deviate from 180°. Morrow *et al*. proposed that this c-axis buckling weakens the Fe-O-Os-O-Fe AFM superexchange interaction, resulting in a prevailing antiparallel Fe-O-Os coupling in all three directions and a FIM ground state [71].

This hypothesis explains the lower T_C observed in $SrCaFeOsO_6$ (T_C = 210 K) compared to Ca_2FeOsO_6 (T_C > 300 K) since the Fe-O-Os bond angle is more severely bent in Ca_2FeOsO_6 [71]. A_2FeOsO_6 compounds (A = Ca, Sr) serve as excellent examples to illustrate the intricate competition of superexchange pathways in 3d-5d double perovskite oxides. The enhanced bending of the Fe-O-Os bond angle suppresses the longer-range superexchange interaction of Fe-O-Os-O-Fe, allowing the nearest neighbor Fe-O-Os AFM coupling to dominate. This complexity in the magnetic ground state of 3d-5d double perovskite oxides contrasts with that of 3d perovskite oxides [100].

Apart from the degree of collinearity between Fe-O-Os bonds, the exchange interaction between Fe and Os can be influenced by various factors. In the case of Sr_2FeOsO_6, Veiga *et al*. reported that the transition from AFM to FIM order can be induced by applying hydrostatic pressure, even without any concurrent symmetric structural changes. The tetragonal lattice of Sr_2FeOsO_6 is maintained under pressure, indicating the absence of a buckling angle in the high-pressure phase [98,101]. Veiga *et al*. demonstrated that the FIM state of Sr_2FeOsO_6 is induced by an increase in the difference between Os and Fe crystal-field splitting ($10Dq_{,Os}$ - $10Dq_{,Fe}$), rather than by bending the Fe-O-Os bonds under pressure. The decrease in lattice parameters and compression of the Fe-Os distance under pressure result in an increase in crystal fields. This increase in crystal fields stabilizes the AFM coupling between Fe and Os along the c-axis. The transition to fully AFM coupling along the c-axis leads to the emergence of ferrimagnetism in the compressed phase of Sr_2FeOsO_6 under pressure (Table 3.2).

The exchange interactions in Sr_2FeOsO_6 can be significantly influenced by pressure, a characteristic strongly linked to the unique nature of the 5d element. This distinction stands in stark contrast to systems that lack 5d elements [102]. It is noteworthy that the FIM phase induced by high pressure up to 40 GPa in Sr_2FeOsO_6 is only 40% of that observed in Ca_2FeOsO_6, as resolved by x-ray magnetic circular dichroism (XMCD) spectroscopy [98].

Table 3.2: Comparison of the structural parameters and physical properties of double perovskite oxides A_2FeOsO_6 (A = Ca, Sr).

	Ca_2FeOsO_6	$SrCaFeOsO_6$	Sr_2FeOsO_6 (AP)	Sr_2FeOsO_6 (HP)
S.G.	$P2_1/n$	$P2_1/n$ (100 K)	$I4/m$	$I4/m$
Bond length of Fe-O (Å)	1.976 × 2 2.020 × 2 2.019 × 2	1.967 × 2 1.982 × 2 2.022 × 2	1.939 × 4 1.936 × 2	
Bond length of Os-O (Å)	1.986 × 2 1.936 × 2 1.946 × 2	1.997 × 2 1.999 × 2 1.941 × 2	1.985 × 4 2.007 × 2	
Bond angle of B-O-Os (deg.)	151.5 154.0 151.7	152.3 150.3 150.7	179.9 180	
Physical properties	Insulator, FIM	FIM	Insulator, AFM	FIM
T_{mag} (K)	320 [15]	210	140, 67	Above R.T.

	350 [71]			(P > 30 GPa)
θ_{Weiss} (K)			+80 [85,97]	
			+24 [71]	
Reference	[15,71]	[71]	[71,85,97]	[98,101]

Similar to A_2FeOsO_6 (A = Ca, Sr), the substitution of Ca with Sr in the Co-Os and Ni-Os double perovskite oxides A_2BOsO_6 (A = Ca, Sr; B = Co, Ni) also leads to a transition from FIM to AFM ordering. Ca_2CoOsO_6 and Ca_2NiOsO_6 exhibit insulating and FIM properties with Curie temperatures of 145 K and 175 K, respectively [46,103], which are lower than the observed T_C in Ca_2FeOsO_6. The electronic analogues of these compounds, Sr_2CoOsO_6 and Sr_2NiOsO_6, are both AFM insulators [34,36]. The structural and physical properties of the Co-Os and Ni-Os double perovskite oxides are presented in Table 3.3.

Despite both compounds being insulators, the conductivity of Ca_2NiOsO_6 is 2-3 orders of magnitude lower than that of Ca_2CoOsO_6 [103]. This difference in conductivity can be attributed to the variations in the filling of the 3d orbitals. However, the magnetic ordering in both FIM insulator compounds remains similar. XMCD studies have revealed the FM coupling between Os-Os through the Os-O-O-Os exchange pathway [103]. Morrow *et al*. demonstrated that the primary driving force towards the FIM state in Ca_2CoOsO_6 and Ca_2NiOsO_6 is the AFM Os-O-Co/Ni superexchange coupling, which involves virtual hopping between partially filled t_{2g} orbitals of Os and half-filled e_g orbitals of Co or Ni. In the case of Sr_2CoOsO_6 and Sr_2NiOsO_6, where the bond angle of Os-O-Co/Ni approaches linearity, t_{2g}-e_g coupling is forbidden. As a result, both Sr_2CoOsO_6 and Sr_2NiOsO_6 exhibit AFM states instead of FIM states [103]. The sensitivity of magnetic interactions in Co-Os double perovskite compounds to changes in the Co-O-Os bond angles is further demonstrated by the substitution case of $SrCaCoOsO_6$ [104].

Regarding the AFM compound Sr_2CoOsO_6, neutron diffraction studies have revealed different ground states for the magnetic sublattices of Co and Os [44,104,105]. Consequently, Sr_2CoOsO_6 exhibits two magnetic transition temperatures. Below 108 K (T_{N1}), AFM ordering of Os^{6+} occurs, while high-spin Co^{2+} orders antiferromagnetically below 70 K (T_{N2}) [44]. Yan *et al*. suggested that in the first AFM state, the magnetic moments of Co^{2+} and Os^{6+} dynamically fluctuate, while their average effective moments (μ_{eff}) exhibit long-range order [105]. Furthermore, below T_{N2}, the magnetic moments of Co^{2+} become frozen, resulting in a noncollinear spin-canted AFM state [105]. In contrast, the moments of Os^{6+} freeze into a randomly canted state at an even lower temperature, approximately 5 K [105]. These observations indicate weak coupling between the Co and Os sublattices in the double perovskite Sr_2CoOsO_6.

Although both Sr_2CoOsO_6 and Sr_2NiOsO_6 exhibit AFM ordering, the exchange interactions in these compounds may not be exactly the same. This is evidenced by the different signs of the Weiss temperatures (θ_{Weiss}): a negative value for Sr_2CoOsO_6 and a positive value for Sr_2NiOsO_6, as shown in Table 3.3. The positive θ_{Weiss} suggests a net FM interaction in Sr_2NiOsO_6 [46]. The FM interaction is even stronger in the cubic double perovskite Ba_2NiOsO_6, as indicated by the increase in θ_{Weiss} from 27 K to 113 K. This strong FM interaction results in FM ordering above 100 K [16]. Fig. 3.3 provides a comparison of the magnetic properties of the three Ni-Os double perovskite oxides.

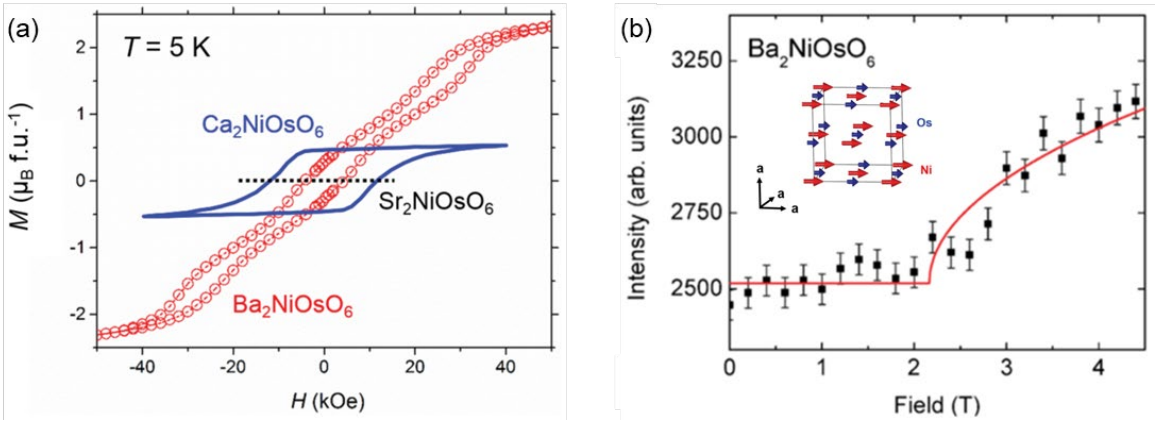

Fig. 3.3: (a) Isothermal magnetization loop of Ba_2NiOsO_6 at 5 K in comparison with the loops for ferrimagnetic Ca_2NiOsO_6 and antiferromagnetic Sr_2NiOsO_6. (b) Magnetic field dependence of the intensity of the magnetic peak of Ba_2NiOsO_6 , with the inset showing the magnetic order model of the ferromagnetic state of Ba_2NiOsO_6 based on the neutron diffraction analysis [16]. Reprinted with permission from [Feng, H. L., *et al*., Phys. Rev. B, 94 (23), 235158, 2016] Copyright (2016) by the American Physical Society.

The substitution of larger alkaline earth ions at the A-site leads to an increase in the tolerance factor for the double perovskite structure. Ba_2NiOsO_6, for instance, exhibits a tolerance factor greater than 1. However, the stabilization of the rock-salt double perovskite phase in Ba_2NiOsO_6 requires high-pressure conditions [16]. This cubic double perovskite compound displays intriguing properties, as it is a FM semiconductor and exhibits metamagnetic behavior. At approximately 32 K, the application of a weak external magnetic field induces an antiferromagnetic-like transition in Ba_2NiOsO_6. Furthermore, around 100 K, it undergoes a transition to a FM insulating state. Neutron diffraction studies have confirmed the transition from a modulated AFM state to a collinear FM state under a magnetic field of 21 kOe at 5 K. Notably, the insulating property persists in both magnetic states [16]. Theoretical calculations, as illustrated in Fig. 3.4, suggest that SOC plays a significant role in generating a charge gap and contributing to the insulating nature of Ba_2NiOsO_6 [16].

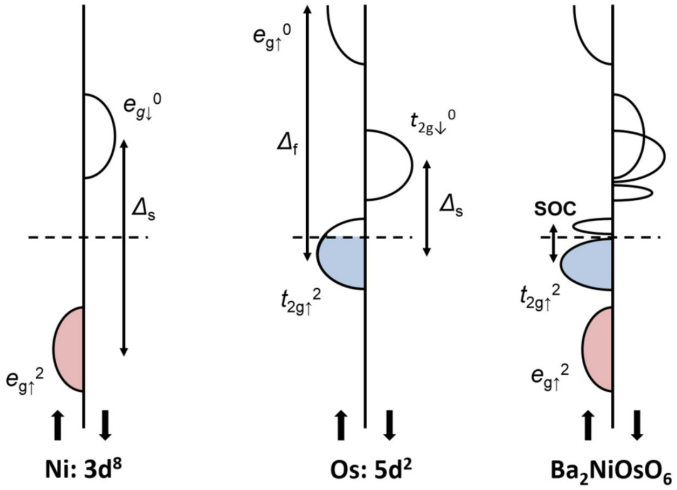

Fig. 3.4: A schematic representation of the density of states structure of the d-band in the ferromagnetic state of Ba_2NiOsO_6 [16]. Reprinted with permission from [Feng, H. L., *et al*., Phys. Rev. B, 94 (23), 235158, 2016] Copyright (2016) by the American Physical Society.

Table 3.3: Comparison of the structural parameters and physical properties of double perovskite A_2BOsO_6 (A = Ca, Sr, Ba; B = Co, Ni).

	Ca_2CoOsO_6	Sr_2CoOsO_6	Ca_2NiOsO_6	Sr_2NiOsO_6	Ba_2NiOsO_6
S.G.	$P2_1/n$	$I4/m$	$P2_1/n$	$I4/m$	Fm-3m
Bond length of B-O (Å)	2.076 × 2 2.063 × 2 2.031 × 2	2.0379 × 4 2.052 × 2	2.024 × 2 2.058 × 2 2.066 × 2	2.032 × 4 2.055 × 2	2.078 × 6
Bond length of Os-O (Å)	1.934 × 2 1.936 × 2 1.929 × 2	1.9151 × 4 1.927 × 2	1.924 × 2 1.928 × 2 1.922 × 2	1.910 × 4 1.906 × 2	1.943 × 6
Bond angle of B-O-Os (deg.)	149.86 150.97 150.78	165.83 180	150.97 150.59 150.53	165.85 180	180
Tolerance factor [a]	0.93	0.98	0.93	0.99	1.05
BVS at B site [b]	2.24	2.33	2.18	2.24	2.02
BVS at Os site [b]	5.55	5.76	5.68	5.93	5.41
Physical properties	Insulator, FIM	Insulator, AFM	Insulator, FIM	Insulator, AFM	Insulator, FM
T_{mag} (K)	145	108, 70	175	50	100, 32
θ_{Weiss} (K)	+5	-51		+27	+113
Reference	[104]	[44,105]	[46,103]	[46]	[16]

[a] Tolerance factor and the global instability index (GII) are calculated by SPuDS version 2.21.05.11.

[b] BVS $= \sum_{i=1}^{N} v_i$, where $v_i = e^{(R_0 - l_i)/B}$, N is the coordination number, l is the bond length, B = 0.37.

3.1.4 Properties of Os-based double perovskite oxide with A = Pb

The high-pressure synthesis technique allows for the stabilization of various osmate double perovskites with lead (Pb) at the A-site, as summarized in Table 3.4. Despite having tolerance factors close to 1, these compounds do not adopt cubic or tetragonal structures. Instead, they crystallize into a monoclinic lattice structure. The application of high-pressure conditions in these cases likely inhibits the formation of competing phases, such as the pyrochlore $Pb_2BOsO_{7-\delta}$. Additionally, a related compound, Pb_2CaOsO_6, has been synthesized under similar high-pressure conditions. However, it does not crystallize into the standard rock-salt double perovskite structure. Instead, it adopts a highly distorted monoclinic structure characterized by lattice parameters a = 10.0812(3) Å, b = 5.689(1) Å, c = 11.837(4) Å, and β = 125.32(2)° at 2 K. This distorted lattice structure persists even at high temperatures [39].

Table 3.4: Comparison of the structural parameters and physical properties of double perovskite Pb_2BOsO_6 (B = Co, Ni, Zn).

	Pb_2CoOsO_6 (Room temp.)	Pb_2NiOsO_6 (Room temp.)	Pb_2ZnOsO_6 (T = 2 K)
S.G.	$P2_1/n$	$P2_1/n$	$P2_1/n$
Bond length of B-O (Å)	1.9027 × 2 2.1084 × 2 2.2409 × 2	2.01 × 2 1.98 × 2 2.275 × 2	2.022 × 2 2.202 × 2 2.177 × 2
Bond length of Os-O (Å)	1.8258 × 2 1.8857 × 2	1.95 × 2 1.99 × 2	2.007 × 2 1.836 × 2

	2.1119 × 2	1.841 × 2	1.878 × 2
Bond angle of B-O-Os (deg.)	172.2 168.1 145.4	179.5 175.4 147.1	158.62 159.33 156.88
Tolerance factor [a]	1.004	1.008	1.000
BVS at B site [b]	2.19	2.08	1.92
BVS at Os site [b]	6.05	5.91	6.06
Physical properties	Metal, AFM	Metal, AFM	Metal, paramagnetic
T_N (K)	45	58	
θ_{Weiss} (K)	-106	-102	+214.4
Reference	[18]	[38]	[39]

[a] Tolerance factor and the global instability index (GII) are calculated by SPuDS version 2.21.05.11.

[b] BVS $= \sum_{i=1}^{N} v_i$, where $v_i = e^{(R_0 - l_i)/B}$, N is the coordination number, l is the bond length, $B = 0.37$.

In most osmate double perovskite oxides, the dominant property is insulating behavior. However, osmate double perovskites with Pb at the A-site exhibit contrasting electronic properties. Compounds such as Pb_2BOsO_6 (B = Co, Ni, Zn) display metallic behavior down to the lowest temperatures [18,38,39]. Pb_2CaOsO_6 undergoes a metal-insulator transition accompanied by an AFM transition [39].

Antiferroelectric-like displacements of Pb from the center of the oxygen polyhedron have been observed in Pb_2CaOsO_6 [39]. While it is not uncommon for Pb^{2+}-based perovskite insulators to exhibit lone pair electronic instability, it is rare to observe this phenomenon in a metallic phase. Below 80 K, a metal-to-insulator transition occurs in Pb_2CaOsO_6, accompanied by the onset of AFM order. Jacobsen *et al*. proposed that the metal-insulator transition in Pb_2CaOsO_6, driven by spin ordering, can be attributed to a Slater transition [39].

Similar phase transitions with inversion symmetry breaking induced by AFM ordering have been observed in metallic Pb_2CoOsO_6 and Pb_2NiOsO_6 [18,38]. In both compounds, a subtle spin-driven structural transition occurs from centrosymmetry to noncentrosymmetry. This transition is analogous to type-II multiferroics, where the establishment of magnetic order leads to the emergence of ferroelectricity. The coexistence of the polar phase and metallic behavior in Pb_2CoOsO_6 and Pb_2NiOsO_6 categorizes them as polar metals. Notably, the first known example of a polar metal was discovered in $LiOsO_3$, an osmate oxide [50]. The polar phase in $LiOsO_3$ can be induced by changes in temperature or pressure [106,107]. Jiao *et al*. performed transport measurements on Pb_2CoOsO_6 under pressures up to 11 GPa and found that the AFM polar metal state observed at ambient pressure can be suppressed with increasing pressure. This suppression leads to the emergence of a new centrosymmetric AFM state above a critical pressure [108].

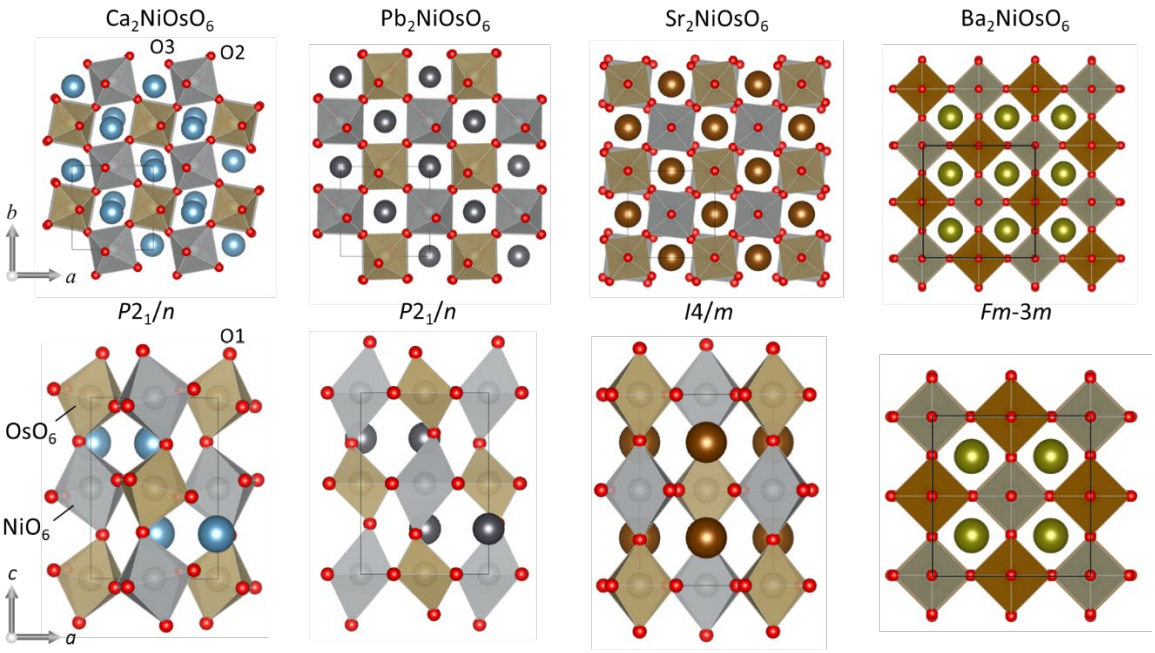

Fig. 3.5: Comparison of the crystal structures between Pb_2NiOsO_6 and A_2NiOsO_6 (A = Ca, Sr, and Ba).

The structure of Pb_2NiOsO_6 is compared to its analogues A_2NiOsO_6 (A = Ca, Sr, Ba), as depicted in Fig. 3.5. As the ionic radius at the A-site of the double perovskite A_2BOsO_6 (A = Ca, Pb, Sr, Ba) increases, the lattice structure undergoes a transformation from monoclinic to tetragonal and eventually to cubic. With the ionic radius of Pb^{2+} falling between that of Ca^{2+} and Sr^{2+}, Pb_2NiOsO_6 adopts a monoclinic lattice structure that closely resembles the A_2NiOsO_6 compound family. However, a notable difference in octahedral distortion can be observed when comparing the local distortions of Pb_2NiOsO_6 with its analogues A_2NiOsO_6 (A = Ca, Sr, Ba).

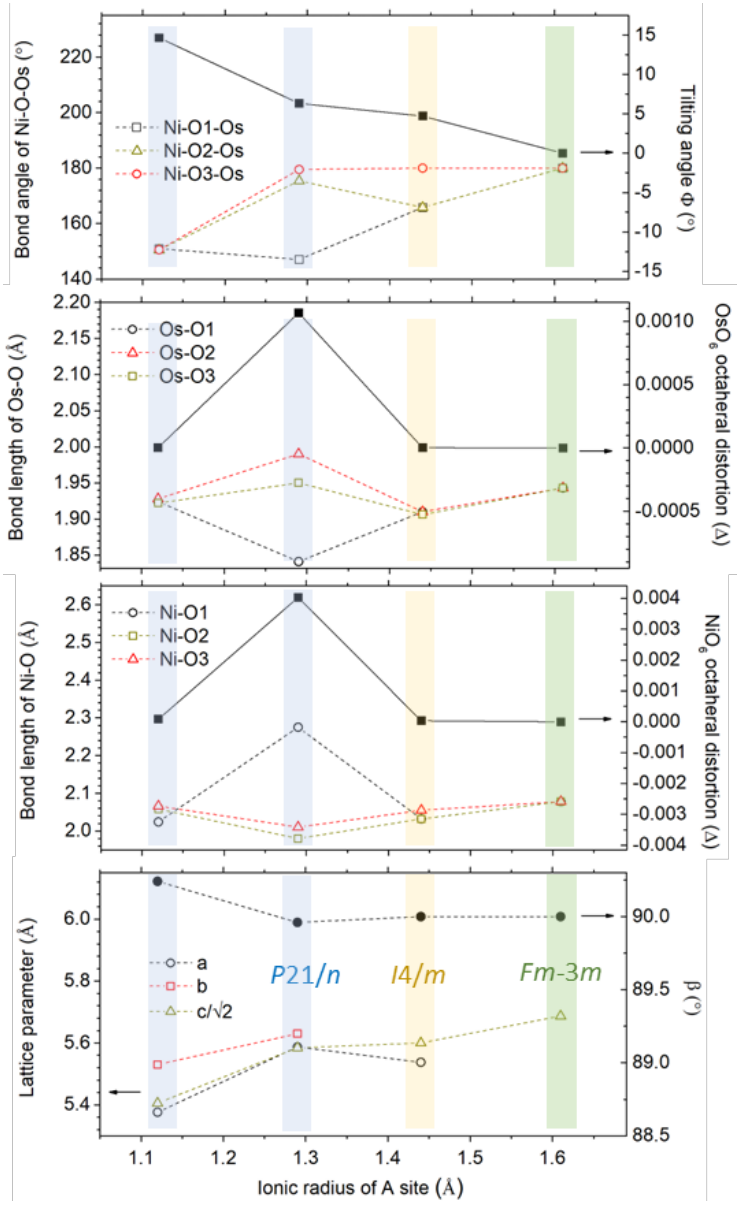

Fig. 3.6: Variations in lattice parameter, bond length and bond angle in double perovskite A_2NiOsO_6 (A = Ca, Pb, Sr, Ba). The data are extracted from references [16,38,46].

The octahedral distortions (Δ) in the double perovskite structure can be calculated using the formula mentioned in the paper [52]:

$$\Delta = \frac{1}{6}\sum_{i=1}^{6}\left(\frac{d_i - d_{av}}{d_{av}}\right)^2.$$

Here, d_i represents the bond length of B-O and B'-O, and d_{av} is the average bond length. The tilting angle (Φ) can be estimated from the average bond angle (θ) of B-O-B' using the formula $\Phi = (180 - \theta)/2$. The variation of structural parameters with the A-site cation radius is depicted in Fig. 3.6. While the Φ shows a continuous change corresponding to the ionic radius of the A-site cation in the A_2NiOsO_6 series, there is a notable difference in the bond angles of Ni-O-Os in Pb_2NiOsO_6. Specifically, the bond angle of Ni-O1-Os, which is nearly aligned with the c-axis as shown in Fig. 3.5, is significantly smaller compared to the other two Ni-O2/O3-Os angles that lie approximately in the ab-plane. Moreover, in Pb_2NiOsO_6, both the octahedral distortion (Δ) of OsO_6 and NiO_6 are notably enhanced compared to A_2NiOsO_6 (A = Ca, Sr, Ba). A similar enhanced octahedral distortion

can also be observed in Pb_2CoOsO_6 when compared to Ca_2CoOsO_6 and Sr_2CoOsO_6. The presence of Pb^{2+} with a lone pair occupying the A-site appears to have a significant influence on the local distortion within the double perovskite structure.

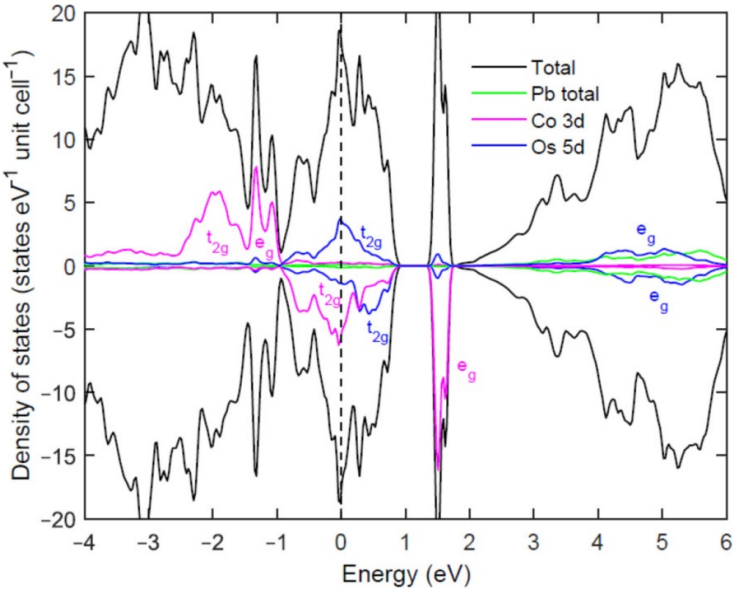

Fig. 3.7: Total and projected spin-polarized partial density of states for antiferromagnetic Pb_2CoOsO_6 calculated using the generalized gradient approximation [18]. Reprinted with permission from [Princep, A. J., *et al*., Phys. Rev. B, 102 (10), 104410, 2020] Copyright (2020) by the American Physical Society.

The origin of the metallic properties observed in Pb_2BOsO_6 (B = Co, Ni, Zn) is still not fully understood. First-principles calculations suggest that the density of states at the Fermi level is predominantly contributed by the d-electrons of the 3d element and Os in both Pb_2NiOsO_6 and Pb_2CoOsO_6 (Fig. 3.7) [18,38]. This is reminiscent of the metallic phase of perovskite $BiNiO_3$, where the presence of a lone pair on Bi^{3+} and the dominant contribution of the d-band of Ni at the Fermi level are also observed [109].

Pb_2NiOsO_6 and Pb_2CoOsO_6, as AFM metallic oxides with a three-dimensional structure, are unique as 3d-5d mixed systems. The application of hydrostatic pressure offers the possibility to tune the bandwidth of simple perovskites, especially those consisting of only one 3d element. By measuring the electron transport and magnetic properties under pressure, valuable information can be obtained regarding the nature of the material.

According to Bloch's rule, there is a relationship between the T_N and the cell volume of AFM insulators [110]. T_N can be enhanced by reducing the cell volume through the application of pressure, as observed in localized-electron systems such as $YCrO_3$ and $CaMnO_3$ [111]. In contrast, the application of pressure on the AFM metal $CaCrO_3$ leads to a reduction in its T_N [112,113]. Jiao *et al*. demonstrated that the AFM metal Pb_2CoOsO_6 exhibits an increase in T_N, as determined from the resistivity anomaly, under applied pressure [108]. The behavior of Pb_2CoOsO_6 under pressure differs from that of AFM insulators like $YCrO_3$ and $CaMnO_3$, as well as the AFM metal $CaCrO_3$. In contrast, Sr_2FeOsO_6, another osmate double perovskite, exhibits behavior expected for a localized Mott-insulating system, where the magnetic ordering temperature increases with increasing pressure [101]. In this regard, the effect of pressure on 3d-5d mixed systems has not been extensively

investigated, and it appears that the combination of 3d and 5d elements in the same system poses additional challenges for understanding their behavior under pressure.

3.1.5 Properties of the Re or Os-based double perovskite with *B* = a non-magnetic element

The B-site occupied by non-magnetic cations forms an important group in 5d double perovskite oxides, as listed in Table 3.5. Among them, there is a growing interest in certain cubic 5d double perovskite oxides that incorporate alkali or alkaline earth ions, as well as Y^{3+} and Zn^{2+} ions, at the B site. For instance, cubic Re or Os-based double perovskites with the electronic configuration $5d^1$ or $5d^2$, such as Ba_2NaOsO_6, Ba_2BOsO_6 (*B* = Zn, Mg, Ca), Ba_2MgReO_6, and Ba_2YReO_6, serve as promising platforms for exploring multipolar magnetism. The exploration of multipolar magnetism in these materials can provide valuable insights into the behavior of quantum magnets.

On the other hand, an epitaxial film of the double perovskite Sr_3OsO_6 exhibits ferromagnetism at temperatures exceeding 1000 K [61], while the bulk form of the same composition is dominated by antiferromagnetism [49]. The underlying reasons for such a remarkably high magnetic transition temperature observed in the double perovskite film remain a mystery and require further investigation [114].

In solid materials, conventional broken symmetry phases typically involve the magnetic dipole moment of electrons. However, in certain solid systems, broken symmetry can arise from higher-order multipolar degrees of freedom. Extensive theoretical and experimental investigations have been conducted on multipolar orders in f-orbital compounds [115,116]. In recent years, there has been a growing interest in exploring the occurrence of multipolar orders in 5d oxides that exhibit strong SOC [117-119]. Re and Os-based cubic double perovskites are particularly significant in this category due to their high local symmetry, strong SOC, presence of localized electrons, and the weakly correlated nature of 5d metals [120-122].

The multipolar order is known as the hidden order since it is generally subtle and hard to detect by traditional experimental probes. Nuclear magnetic resonance studies have experimentally confirmed that Ba_2NaOsO_6 with a $5d^1$ configuration exhibits a specific type of canted FM state [123,124]. This state is characterized by the presence of two sub-lattice magnetizations, and the magnetic order is accompanied by a structural change. Interestingly, the breaking of cubic symmetry occurs prior to the onset of magnetic order [124]. The exotic canted two-sublattice FM state observed in Ba_2NaOsO_6 is believed to be driven by the staggered quadrupolar order [125]. Quadrupolar order has also been observed in another double perovskite with a $5d^1$ configuration, Ba_2MgReO_6 [126]. The first identified candidate for d-orbital octupolar order was found in the cubic osmate double perovskites Ba_2BOsO_6 (*B* = Zn, Mg, Ca) [121]. These compounds possess a $5d^2$ electron configuration. In contrast to Ba_2NaOsO_6 and Ba_2MgReO_6, where a structural change precedes quadrupolar order, there is no deviation from cubic symmetry observed in Ba_2BOsO_6 (*B* = Zn, Mg, Ca) [121]. Through magnetic neutron powder diffraction, inelastic neutron scattering, and high angular resolution synchrotron x-ray diffraction measurements performed on Ba_2BOsO_6 (*B* = Zn, Mg, Ca) along with theoretical calculations, it has been suggested that these $5d^2$ cubic perovskites exhibit ferro-octupolar order at low temperature [121,122].

The multipolar order observed in cubic double perovskites is distinctively different from their electronic counterparts that crystallize in noncubic structures. For example, Sr_2MgOsO_6 exhibits conventional AFM ground states [53,127]. The comprehensive understanding of multipolar

order in Re-based and Os-based cubic double perovskites is still an ongoing area of research that continues to attract increasing interest in both experimental and theoretical investigations [120,128-131].

Table 3.5: Experimental data and properties of Re-based and Os-based cubic double perovskites with non-magnetic elements at the B site.

Electronic configuration, compound		synthesis pressure	t [a]	GII [a]	Physical properties	T_{mag} (K)	θ_{Weiss} (K)	μ_{eff} (μ_B)	Ref.
5d^0	Ba_2LiReO_6	AP [c]	1.0398	0.35824	-	-	-	-	[132]
	Ba_2NaReO_6	AP	0.9592	0.32403	-	-	-	-	[132]
	$K_2NaOsO_{5.5}$ [b]	AP	1.0226	0.23158	Diamagnetic	-	-	-	[133]
5d^1	Ba_2MgReO_6 [d]	AP	1.0298	0.26410	FM	18	20.8	0.496	[134]
					Spin–orbit coupled Mott insulator, quadrupolar order (33 K), dipolar order (18 K)	33, 18	-14.6, -15.2, -11.2	0.678, 0.689, 0.673	[126]
					Canted AFM	18	-	-	[120]
	Ba_2CaReO_6	AP	0.9645	0.27768	AFM	15.4	-38.8	0.744	[135]
					AFM	16	-41.5	0.700	[136]
	Ba_2ZnReO_6	AP	1.0270	0.23662	FM	11	-66	0.940	[134]
					Insulator, canted FM	16	-3.1	0.7141	[41]
	Ba_2CdReO_6 [e]	AP	0.9788	0.17659	Insulator, AFM	4	-65.8	1.04	[41]
					Quadrupole order (25 K), canted AFM (12 K)	25, 12	-15.3	0.720	[137]
	Ba_2LiOsO_6	AP	1.0737	0.72101	AFM	8	-40.48	0.733	[138]
					AFM, spin-flop transition	8	-	-	[139]
					AFM	-	-55.7	0.897	[41]
	Ba_2NaOsO_6 [f]	AP	0.9879	0.14779	FM-like order	8	-32.45	0.677	[138]
					Mott insulator, FM	6.8	-10, -10, -13	0.602, 0.596, 0.647	[140]
					FM	7.2	-	-	[139]
					Canted FM, quadrupolar order	~10	-	-	[123]
					Canted FM	7	-41.7	0.844	[41]
5d^2	Ba_2YReO_6 [g]	AP	0.9912	0.08291	AFM	31	-726	2.32	[141]
					Spin freezing	50, 25	-616	1.93	[142]
					Ordered with reduced dipole moment	-	-	-	[128]
	Sr_2CaOsO_6	AP	0.9194	0.51124	-	-	-198	1.68	[143]
	Ba_2CaOsO_6	AP	0.9746	0.21372	AFM	51	-157	1.61	[135]
					AFM	50	-156.2	1.640	[144]
					Ferro-octupolar order	49			[121]
	Ba_2MgOsO_6	AP	1.0414	0.37790	AFM	51	-120	1.536	[145]
					Ferro-octupolar order	51			[121]
	Ba_2ZnOsO_6	AP	1.0385	0.34785	AFM	~30	-149	1.947	[145]
					Ferro-octupolar order	30			[121]
	Ba_2CdOsO_6	AP	0.9892	0.10348	No magnetic ordering	-	-117.7	1.972	[145]
5d^3	Ba_2InOsO_6	AP	1.0127	0.10293	Insulator, AFM	28	-155		[42]
	Ba_2ScOsO_6	AP	1.0259	0.22664	Insulator, AFM	93	-590		[42]
	Ba_2YOsO_6	AP	0.9858	0.12196	AFM	69.65	-717	3.93	[43]
		6 GPa			AFM	69	-571	3.52	[42]

[a] Tolerance factor and the global instability index (GII) are calculated by SPuDS version 2.21.05.11.

[b] The reference suggests an oxidation state of +8 for Os in $K_2NaOsO_{5.5}$ [133]. Due to the lack of an effective ionic radius for Os^{8+} in a six-coordinate environment, the tolerance factor is calculated using the ionic radius data from Os^{7+}.

[c] AP denotes ambient pressure.

[d] In reference [134], a Weiss temperature of -373 K was obtained by fitting the temperature range of approximately 200 to 300 K. Additionally, applying the Curie-Weiss fitting to a narrower temperature range of approximately 22 to 40 K yielded a θ_{Weiss} of 20.8 K and an μ_{eff} of 0.496 μ_B. The table presents three values for μ_{eff} and θ_{Weiss} for single crystal Ba_2MgReO_6, which were determined based on data collected with magnetic fields oriented in the [100], [110], and [111] directions [126].

[e] The μ_{eff} and θ_{Weiss} for Ba_2CdReO_6 obtained by fitting the data between T_q (quadrupole order) and T_m (magnetic order) are 0.50 μ_B and 10.3 K [137].

[f] The table presents three values for μ_{eff} and θ_{Weiss} for single crystal Ba_2NaOsO_6, which were determined based on data collected with magnetic fields oriented in the [100], [111], and [110] directions [140]. The reference [123] deduced the transition temperature of around 10 K into the canted FM phase based on the nuclear magnetic resonance data.

[g] In reference [141], the crystal structure of Ba_2YReO_6 is reported as a $P2_1/n$ monoclinic structure. In contrast, other references listed in the table suggest that the crystal structure is a cubic double perovskite structure.

3.1.6 Other Re and Os-based double perovskite oxides

In the realm of oxides, the $A_2BB'O_6$ double perovskite structure accommodates a wide variety of cations at the A and B sites, making it a large family of compounds. While this section focuses specifically on double perovskites with B' = Re and Os, it is challenging to encompass all the compounds within this category. In previous sub-sections, several families of Re or Os-based double perovskites have been discussed in more detail due to their extensive study or growing interest in recent years. However, to provide a comprehensive research overview, we have included tables summarizing other experimentally reported Re and Os-based double perovskites in this section. The S.G. of the double perovskites listed in Table 3.6 and Table 3.7 were determined at room temperature, and for those not determined at room temperature, the temperature conditions are noted. The properties for each compound include the electronic and magnetic properties confirmed by experimental studies, excluding those solely suggested by theoretical simulations.

Table 3.6: Experimentally reported Re-based double perovskite oxides.

Re valence state, compound	Pressure of synthesis	S. G. [a]	t [b]	GII [b]	Properties	T_{mag} (K)	Refs
Re^{5+} ($5d^2$)							
Sr_2ScReO_6	AP	$P2_1/n$	0.9732	0.00012	Insulator, AFM	75	63,146
Sr_2YReO_6	AP	$P2_1/n$	0.9350	0.00637	Spin glass	12	147
					AFM with weak FM component	6	148
Sr_2InReO_6	AP	$P2_1/n$	0.9606	0.00076	Insulator, magnetically frustrated system lacking long-range order	-	149
					Insulator, nonmagnetic singlet ground state		147
Sr_2TbReO_6	AP	$P2_1/n$	0.9311	0.00739	AFM	2.6	148
Sr_2DyReO_6		$P2_1/n$	0.9348	0.00642	FM ordering of Dy moments	5, 93	
Sr_2HoReO_6		$P2_1/n$	0.9371	0.00512	paramagnetic	-	
Sr_2ErReO_6		$P2_1/n$	0.9359	0.00589	paramagnetic	-	
Sr_2TmReO_6		$P2_1/n$	0.9382	0.00566	paramagnetic	-	
Sr_2YbReO_6		$P2_1/n$	0.9415	0.00429	AFM dominant	20	
Sr_2LuReO_6		$P2_1/n$	0.9447	0.00383	AFM with weak FM component	12	
Ba_2NdReO_6	AP	$P2_1/n$	0.9751	0.00034	AFM	100	141

Ba_2SmReO_6		$P2_1/n$	0.9741	0.00053	AFM	82	
Ba_2EuReO_6		$P2_1/n$	0.9922	0.00004	paramagnetic	-	
Ba_2GdReO_6		$P2_1/n$	0.9871	0.00019	AFM	65	
Ba_2TbReO_6		$P2_1/n$	0.9870	0.00015	AFM	2.4, 29	
Ba_2DyReO_6		$P2_1/n$	0.9909	0.00025	AFM	70	
Ba_2HoReO_6		$P2_1/n$	0.9934	0.00021	AFM	27	
Ba_2ErReO_6		$P2_1/n$	0.9922	0.00004	paramagnetic	-	
Ba_2TmReO_6		$P2_1/n$	0.9945	0.00016	paramagnetic	-	
Ba_2YbReO_6		$P2_1/n$	0.9981	0.00012	paramagnetic	-	
Ba_2LuReO_6		$P2_1/n$			AFM	33	
Mn_2MnReO_6 [c]	5 GPa	$P2_1/n$	0.8778/ 0.8368	0.01718 /0.0437 9	Insulator, AFM, canted AFM	~110, ~50	35
	8 GPa					109, 99	34
La_2LiReO_6	AP	$P2_1/n$	0.9429	0.00280	Spin freezing	~50	142
Pb_2MnReO_6 [c]	AP	$P2_1/n$	1.0166/ 0.9692	0.10205 /0.0002 2	Insulator, FIM	~100	150
		$C2/m$					151
Pb_2NiReO_6	6 GPa	$I2/m$	0.9968	0.00101	FIM, spin glass	37	52
Re^{6+} ($5d^1$)							
Ca_2MgReO_6	AP	$P2_1/n$	0.9187	0.00868	Canted AFM	~20	152
Ca_3ReO_6	AP	$P2_1/n$	0.8605	0.04400	-	-	153
Ca_2MnReO_6 [d]	AP	$P2_1/n$	0.8972	0.01689	Insulator, FM	110	63
					Noncollinear magnetic structure	121	154
Ca_2CoReO_6	AP	$P2_1/n$	0.9189	0.00833	Insulator, FM	130	63
Sr_2MgReO_6 [e]	AP	$I4/m$	0.9714	0.03071	Insulator, AFM	320	63
		$I4/mmm$			Layered AFM	~55	155
Sr_2CaReO_6	AP	$P2_1/n$	0.9099	0.01780	Spin glass	~14	156,157
Sr_2MnReO_6	AP	$P2_1/n$	0.9487	0.00277	Insulator, FM	120	63
					FIM	120	158
					canted magnetic structure	120	159
Sr_2CoReO_6	AP	$I4/m$	0.9717	0.03047	Insulator, AFM	65	63
					AFM	60	45
Sr_2NiReO_6	AP	$I4/m$	0.9758	0.02641	Insulator, FM	18	63
						30	45
Sr_2ZnReO_6	AP	$I4/m$	0.9688	0.03325	Insulator, AFM	20	45,63
Ba_2MnReO_6	AP	Fm-3m	1.0057	0.03994	Insulator, FIM	120	158
					FM	113	40
Ba_2CoReO_6	AP	Fm-3m	1.0300	0.26662	AFM	25	40
						41	160
Ba_2NiReO_6	AP	Fm-3m	1.0344	0.31028	FIM	32	40
Ba_2ZnReO_6	AP	Fm-3m	1.0270	0.23662	Insulator, canted FM	11	134
						16	41
Ba_2CdReO_6	AP	Fm-3m	0.9788	0.17659	Insulator, AFM	4	41
Mn_2CoReO_6 [f]	8 GPa	$P2_1/n$	0.8571	0.02701	Insulator, AFM	94, ~40	32
Mn_2NiReO_6	8 GPa	$P2_1/n$ (150 K)	0.8607	0.02480	Canted AFM	80, 42	33
Pb_2CoReO_6	8 GPa	R-3	0.9926	0.00005	Insulator, AFM	16	51
Re^{7+} ($5d^0$)							
Sr_2LiReO_6 [g]	AP	$I4/m$	0.9809	0.02180	-	-	132,161
Sr_2NaReO_6	AP	$P2_1/n$	0.9049	0.02492	-	-	132
Mn_2LiReO_6	8 GPa	$P2_1/n$	0.8652	0.02871	Weak FM	109	31

[a] The structures listed in the table were determined at or near room temperature according to the literature. Any structures determined at temperatures other than room temperature are indicated in the table.

[b] Tolerance factor (t) and the global instability index (GII) were calculated using SPuDS version 2.21.05.11.

[c] Mixed valent states of $Mn^{2+/3+}$ for the B-site and $Re^{6+/5+}$ for *B*'-site were suggested in ref. [35,151]. Tolerance factor and GII before the slash were calculated with $R_0(Mn^{3+})$ and $R_0(Re^{5+})$, while the latter was calculated with $R_0(Mn^{2+})$ and $R_0(Re^{6+})$. The structure of Pb2MnReO6 at room temperature was determined to be a distorted structure with a monoclinic lattice, and the lattice parameters are a = 18.2309 Å, b = 8.0359 Å, c = 5.7072 Å, and β = 108.288°. It crystallizes into a cubic double perovskite at 523 K [151].

[d] Mixed valent states of Mn and Re were suggested in ref. [162]. Tolerance factor and GII was calculated with $R_0(Mn^{2+})$ and $R_0(Re^{6+})$.

[e] The *I*4/*m* structure was suggested in the references listed in the table, while an earlier literature reported another tetragonal space group, *I*4/*mmm*, for Sr_2MgReO_6 [152].

[f] Mn_2CoReO_6 exhibits complex magnetic properties at low temperatures, and a robust AFM ordering occurs at 94 K, as suggested by ref. [32]. The presence of AFM ordering is indicated in the table. The complex magnetic properties are also observed in Mn_2BReO_6 (*B* = Mn, Fe, Ni), which are not described in detail in the table.

[g] A cubic structure is determined by single-crystal analysis as suggested by reference [132]. However, two other references conducting structure analysis based on polycrystal indicate a tetragonal structure [132,161].

Table 3.7: The experimentally reported Os-based double perovskite oxides.

Os valence state, compound	Pressure of synthesis	S. G. [a]	t [b]	GII [b]	Properties	T_{mag} (K)	Refs
Os^{4+} ($5d^4$) - Os^{5+} ($5d^3$)							
La_2NiOsO_6	AP	$P2_1/n$	0.9480	0.00188	Insulator, FIM	125	[163]
Os^{5+}							
Ca_2InOsO_6	6 GPa	$P2_1/n$	0.9034	0.01326	Insulator, AFM	14	[55]
Ca_2ScOsO_6	AP	$P2_1/n$	0.9152	0.00894	AFM	~69	[164]
Sr_2InOsO_6	AP	$P2_1/n$	0.9553	0.00116	Insulator, AFM	26	[165]
Sr_2ScOsO_6	AP	$P2_1/n$	0.9678	0.00032	Insulator, AFM	92	[165]
Sr_2YOsO_6	AP	$P2_1/n$	0.9300	0.00751	Insulator, AFM	53	[165]
Ba_2NdOsO_6	AP	$P2_1/n$	0.9699	0.00020	Insulator, AFM	65, ~20	[166]
		Fm-3*m*		0.23896	AFM	70	[167]
Ba_2PrOsO_6	AP	*Fm*-3*m*	0.9578	0.32099	AFM	71	[167]
Ba_2SmOsO_6	AP	*Fm*-3*m*	0.9689	0.24623	AFM	65	
Ba_2EuOsO_6	AP	*Fm*-3*m*	0.9558	0.33370	AFM	67	
Ba_2GdOsO_6	AP	*Fm*-3*m*	0.9817	0.15304	AFM	67	
Ba_2TbOsO_6	AP	*Fm*-3*m*	0.9817	0.15362	AFM	2.6	
Ba_2DyOsO_6	AP	*Fm*-3*m*	0.9856	0.12382	Paramagnetic	-	
Ba_2HoOsO_6	AP	*Fm*-3*m*	0.9880	0.10495	AFM	24	
Ba_2ErOsO_6	AP	*Fm*-3*m*	0.9868	0.11447	Paramagnetic	-	
Ba_2TmOsO_6	AP	*Fm*-3*m*	0.9891	0.09613	Paramagnetic	-	
Ba_2YbOsO_6	AP	*Fm*-3*m*	0.9927	0.06797	AFM	2.4	
Ba_2LuOsO_6	AP	*Fm*-3*m*	0.9960	0.04097	AFM	66	
Pb_2FeOsO_6	8 GPa	*Fm*-3*m*	1.0110	0.06712	Insulator, FIM	280	[56]
La_2LiOsO_6	AP	$P2_1/n$	0.9376	0.00397	AFM	39	[168]
La_2NaOsO_6	AP	$P2_1/n$	0.8662	0.05436	Canted AFM	17	[169]
Pr_2LiOsO_6	AP	$P2_1/n$ (150 K)	0.9172	0.01281	AFM	35	[168]
Pr_2NaOsO_6	AP	$P2_1/n$	0.8473	0.07909	AFM, spin-flop transition	7	[169]
Nd_2LiOsO_6	AP	$P2_1/n$	0.9199	0.00778	AFM	23	[168]
Nd_2NaOsO_6	AP	$P2_1/n$	0.8498	0.07015	AFM, spin-flop transition	20, 10	[169]
Sm_2LiOsO_6	AP	$P2_1/n$	0.8999	0.02003	AFM	32	[168]
Os^{6+} ($5d^2$)							
Ca_3OsO_6	6 GPa	$P2_1/n$	0.8695	0.04118	insulator, AFM	50	[14]
Ca_2MgOsO_6	6 GPa	$P2_1/n$	0.9290	0.00616	insulator, spin glass	19	[53]
Ca_2CoOsO_6	AP	$P2_1/n$	0.9293	0.00608	insulator, FIM	145	[103,104]
Sr_3OsO_6	6 GPa	*P*-1	0.8881	-	insulator, AFM	12	[49]

Sr_2MgOsO_6	6 GPa	*I*4/*m*	0.9824	0.02001	insulator, AFM	110	[53]
Sr_2CoOsO_6	AP	*I*4/*m*	0.9826	0.01975	insulator, AFM	108, 70	[44]
Sr_2CuOsO_6	AP	*I*4/*m*	0.9885	0.01337	AFM	18	[170]
Os^{7+} ($5d^1$)							
Sr_2LiOsO_6	6 GPa	*I*4/*m*	1.0129	0.08397	AFM	12	[171]
	AP	*I*4/*m*			spin glass	30	[41]
Sr_2NaOsO_6	AP	$P2_1/n$	0.9320	0.01364	Insulator, canted AFM	~17	[172]

[a] The structures listed in the table were determined at or near room temperature according to the literature. Any structures determined at temperatures other than room temperature are indicated in the table.

[b] Tolerance factor (*t*) and the global instability index (GII) were calculated using SPuDS version 2.21.05.11.

3.2 Ir-based double perovskite oxides

3.2.1 $A_2BIr^{4+}O_6$ (*B* = a nonmagnetic element)

The valence electrons in 3d transition metal oxides typically exhibit strong electron correlations, leading to the formation of the Mott insulating state, primarily characterized by the Hubbard parameter *U* and bandwidth *W*. In contrast, 5d transition metal oxides have more spatially extended 5d orbitals, resulting in relatively stronger hybridization with neighboring orbitals. This leads to a broader bandwidth and lower density of states near the Fermi level, weakening the electronic correlations. Consequently, 5d transition metal oxides are less prone to exhibiting the Mott insulator state compared to 3d transition metal oxides. However, in the case of double perovskite oxides with the general formula $A_2BB'O_6$, even when the *B*' position is occupied by a 5d element, the distance between 5d elements increases when *B* is a different element. This creates an environment that favors the formation of a Mott insulator due to the increased separation between the 5d orbitals.

The double perovskites La_2MgIrO_6 and La_2ZnIrO_6, which were first studied in 1993 [173], have similar crystal structures and electron configurations. However, La_2MgIrO_6 exhibits AFM behavior, while La_2ZnIrO_6 displays weak ferromagnetism. Subsequent neutron scattering experiments have confirmed the presence of long-range AFM ordering in both compounds. Specifically, the magnetic moments in La_2ZnIrO_6 are canted, which explains the observed weak ferromagnetism [174].

In both La_2MgIrO_6 and La_2ZnIrO_6, the SOC effect can split the three t_{2g} orbitals in the octahedral crystal field into an upper doublet with $j = 1/2$ and a lower quadruplet with $j = 3/2$. Theoretical calculations have suggested that the inclusion of a moderate on-site Coulomb repulsion further splits the half-filled $j_{eff} = 1/2$ state, resulting in a Mott insulating state with a narrow gap opening. Therefore, both La_2ZnIrO_6 and La_2MgIrO_6 are considered Mott insulators in which SOC plays a crucial role [174]. Although there are small monoclinic structural distortions at the Ir^{4+} sites, which deviate from perfect cubic crystal fields [168,169], the face-centered cubic (FCC) Kitaev model can still be approximately applied to these materials [175,176].

Similar to La_2MgIrO_6 and La_2ZnIrO_6, Ba_2CeIrO_6 and Sr_2CeIrO_6 exhibit AFM ordering at low temperatures of 17 K and 21 K, respectively. Neutron scattering results for Sr_2CeIrO_6 and Ba_2CeIrO_6 confirm the presence of A-type AFM order in these materials, which was previously observed in La_2ZnIrO_6 [177]. These findings suggest that the magnetic ground state in all four double perovskite iridates originates from a significant AFM Kitaev interaction [178], as the classical phase diagram for the FCC Heisenberg-Kitaev model with $J_{eff} = 1/2$ moments aligns with the observed A-type AFM ordered states in these compounds.

Double perovskite oxides, A_2BIrO$_6$ (A = Pr, Eu, Sn, Nd, Gd), are examples of double perovskite oxides containing a 4f-element on the A-site in combination with a 5d-element on the B'-site [179]. Gd_2ZnIrO_6 and Eu_2ZnIrO_6 exhibit weak canted AFM order below their respective T_N of 23 K and 12 K, similar to La_2ZnIrO_6. Sm_2ZnIrO_6 undergoes AFM ordering at T_N = 13 K. Notably, Nd_2ZnIrO_6 displays complex magnetic properties with indications of magnetic transitions occurring at 16.5 K and 14.5 K, suggesting an intricate interplay between Nd^{3+} and Ir^{4+} [179]. Table 3.8 presents a list of Ir-based double perovskite oxides introduced in this section.

Table 3.8: Summary of space group (S.G.) and magnetic properties of $A_2BIr^{4+}O_6$ (A = Sr, Ba, a rare earth element; B = Zn, Mg).

Material	S.G.	Properties	T_{mag} (K)	μ_{eff} (μ_B/Ir)	θ_{Weiss} (K)	Refs.
La_2ZnIrO_6	$P2_1/n$	AFM	7.5	1.42	-3.1	[174]
Eu_2ZnIrO_6	$P2_1/n$	FM-like	12	-	-	[179]
Nd_2ZnIrO_6	$P2_1/n$	AFM, FM-like	16.5, 14.5	5.6	-40	[179]
Sm_2ZnIrO_6	$P2_1/n$	AFM	13	1.7	7	[179]
Gd_2ZnIrO_6	$P2_1/n$	FM-like	24	11.3	2	[179]
La_2MgIrO_6	$P2_1/n$	AFM	12	1.71	-24	[174]
Pr_2MgIrO_6	$P2_1/n$	AFM	14		-23	[180]
Nd_2MgIrO_6	$P2_1/n$	AFM	12		-25	[180]
Sm_2MgIrO_6	$P2_1/n$	AFM	15			[180]
Eu_2MgIrO_6	$P2_1/n$	AFM	10			[180]
Gd_2MgIrO_6	$P2_1/n$	AFM	3			[180]
Sr_2CeIrO_6	$P2_1/n$	AFM	21			[178]
Ba_2CeIrO_6	Fm-3m	AFM	17			[178]

3.2.2 $A_2BIr^{4+}O_6$ (B = Co, Ni)

In double perovskite oxides $Ln_2BIr^{4+}O_6$ (B = Co, Ni), there are interpenetrating magnetic sublattices consisting of Co^{2+}/Ni^{2+} and Ir^{4+}. The nearest neighbor interaction path is B-O-Ir (B = Co, Ni), and the next nearest neighbor interaction paths are B-O-O-B and Ir-O-O-Ir. Previous reports have indicated that La_2NiIrO_6 and La_2CoIrO_6 exhibit magnetic ordering at temperatures of 110 K and 130 K, respectively [181]. Notably, the magnetic ordering temperatures of La_2NiIrO_6 and La_2CoIrO_6 are approximately one order of magnitude higher than that of La_2ZnIrO_6, suggesting that the strength of magnetic interactions in La_2NiIrO_6 and La_2CoIrO_6 is significantly stronger than in La_2ZnIrO_6. In La_2ZnIrO_6, the dominant magnetic interactions occur through Ir-O-O-Ir. However, in La_2NiIrO_6 and La_2CoIrO_6, the dominant interactions likely take place via the B-O-Ir (B = Ni, Co) path, as cation-anion-anion-cation interactions are generally one order of magnitude weaker than cation-anion-cation interactions [182]. Neutron diffraction studies on La_2NiIrO_6 have revealed that both the Ni and Ir sublattices simultaneously undergo magnetic ordering, resulting in a non-collinear AFM structure [183]. X-ray magnetic circular dichroism studies on La_2CoIrO_6 have shown that Ir^{4+} couples antiferromagnetically to the Co^{2+} sublattice, leading to a weak FM moment [184]. These findings support the notion that the dominant magnetic interactions occur through Ni-O-Ir and Co-O-Ir in La_2NiIrO_6 and La_2CoIrO_6, respectively.

When a magnetic rare-earth element is located on the A-site in Ln_2BIrO$_6$ (Ln = Pr, Nd, Sm,

Eu, Gd, Ho; *B* = Co, Ni) double perovskite oxides, it is common to observe two magnetic transitions. The transitions occurring at high temperatures (above 100 K) correspond to the simultaneous ordering of the Ni/Co and Ir sublattices. On the other hand, the transitions at low temperatures are associated with the ordering of the 4f magnetic moments in the rare-earth sublattices, as these moments have a localized nature. For example, in the case of Nd_2NiIrO_6, studies have shown that the Ni and Ir sublattices exhibit FIM ordering at 125 K. Upon further cooling, the Nd sublattice orders at 7 K, while the magnetic structure of the Ni and Ir sublattices transitions from FIM to AFM. This observation suggests a coupling between the 4f electrons and d electrons, indicating an interaction between them [183]. It is worth noting that the ordering of the rare-earth sublattices takes place independently of the Ni/Co and Ir sublattices, although it can have an influence on the magnetic structures of the latter.

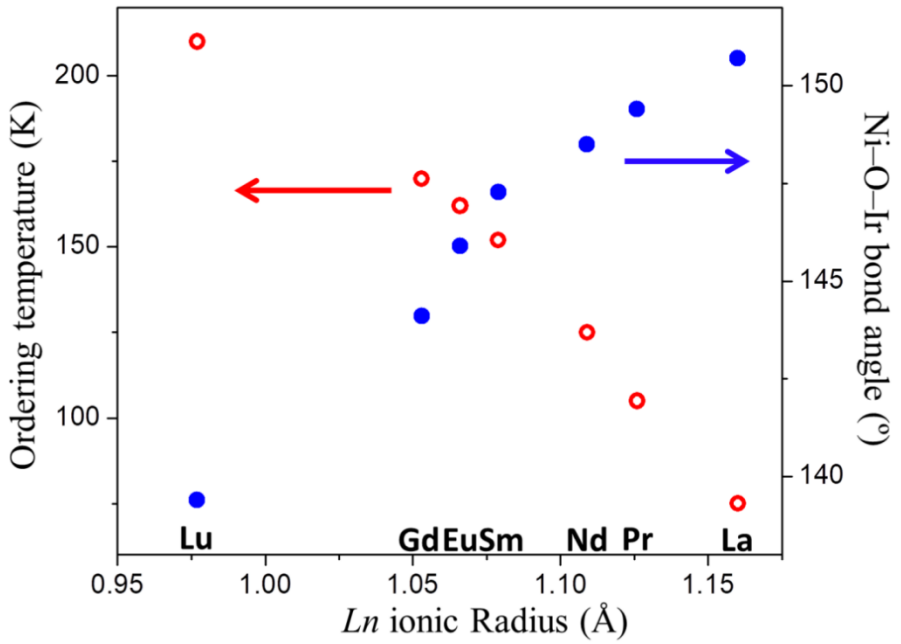

Fig. 3.8: Magnetic transition temperatures and Ni–O–Ir bond angles of the Ln_2NiIrO_6 (*Ln* = La, Pr, Nd, Sm, Eu, Gd, Lu).

Fig. 3.8 illustrates the magnetic ordering temperatures for the Ni and Ir sublattices and the Ni-O-Ir bond angles of Ln_2NiIrO_6 (*Ln* = La, Pr, Nd, Sm-Gd, Lu) [164,172,176,177]. Lu_2NiIrO_6 exhibits the smallest Ni-O-Ir bond angle (resulting in the largest structural distortions) and the highest ordering temperature. On the other hand, La_2NiIrO_6 has the largest Ni-O-Ir bond angle (resulting in the least structural distortions) and the lowest ordering temperature. This clearly demonstrates the structure-property relationship for these Ir-based double perovskites: greater structural distortions lead to higher magnetic ordering temperatures. A similar correlation has also been observed in the Os-based double perovskites $Ca_{2-x}Sr_xFeOsO_6$ [185,186].

The FIM nature of Lu_2NiIrO_6 indicates that the Ni^{2+} and Ir^{4+} are antiferromagnetically coupled, suggesting that the dominant interactions are AFM via Ni^{2+}-O-Ir^{4+} bonds. Since the t_{2g} orbitals of Ni^{2+} are fully filled, the AFM exchange coupling between Ni^{2+} and Ir^{4+} can only occur through virtual hopping between the half-filled Ni-e_g and partially filled Ir-t_{2g} orbitals. In the cubic

double perovskite structure, where the Ni^{2+}-O-Ir^{4+} pathway is linear, the Ni-e_g and Ir-t_{2g} orbitals are orthogonal and hopping between them is not possible. However, in the distorted double perovskites where the Ni^{2+}-O-Ir^{4+} bond angles deviate significantly from 180°, hopping between Ni-e_g and Ir-t_{2g} orbitals becomes feasible [187]. As the structural distortion increases, the AFM exchange coupling between the half-filled Ni-e_g and partially filled Ir-t_{2g} orbitals is expected to strengthen, which could potentially result in higher magnetic ordering temperatures.

Ln_2CoIrO_6 (*Ln* = La, Eu, Tb, Ho) [184,188] exhibit a similar structural-property relationship as the Ni series of Ir double perovskites. La_2CoIrO_6, which has the largest A-site cation, exhibits the lowest magnetic ordering temperature. On the other hand, Ho_2CoIrO_6, with the smallest A-site cation, shows the highest magnetic ordering temperature (refer to Table 3.9).

Table 3.9: Summary of space group (S.G.) and magnetic properties of $Ln_2BIr^{4+}O_6$ (*Ln* = a rare earth element; *B* = Ni, Co).

Material	S.G.	Properties	T_{mag} (K)	μ_{eff} (μ_B/Ir)	θ_{Weiss} (K)	Refs.
La_2CoIrO_6	$P2_1/n$	FIM	90	4.5	36	[184]
Eu_2CoIrO_6	$P2_1/n$		105	5.5	-5	[188]
Tb_2CoIrO_6	$P2_1/n$		117, 10	14.7	-7	[188]
Ho_2CoIrO_6	$P2_1/n$		123, 13	15.9	-3	[188]
La_2NiIrO_6	$P2_1/n$	AFM	75	3.28	0.35	[181]
Pr_2NiIrO_6	$P2_1/n$	FM	105, 4	4.84		[183]
Nd_2NiIrO_6	$P2_1/n$	FM	125, 7	6.19		[183]
Sm_2NiIrO_6	$P2_1/n$	FM	152			[183]
Eu_2NiIrO_6	$P2_1/n$	FM	162			[183]
Gd_2NiIrO_6	$P2_1/n$	FM	170	11.35		[183]
Lu_2NiIrO_6	$P2_1/n$	FM	207	3.47	-37	[189]

3.2.3 $A_2BIr^{5+}O_6$ (*B* = a nonmagnetic element)

Ir, in its pentavalent state, is characterized by a $5d^4$ electronic configuration. The strong SOC present in these systems causes the splitting of the three t_{2g} orbitals in the octahedral crystal field into an upper doublet with total angular momentum $j = 1/2$ and a lower quadruplet with $j = 3/2$ [190]. In the case of the tetravalent iridate Sr_2IrO_4 (Ir^{4+}: $5d^5$), the ground state is attributed to the SOC-assisted Mott-insulating state with $J_{eff} = 1/2$ [190]. When there are four 5d electrons occupying the lower quadruplet, the ground state for Ir^{4+} is expected to have $j = 0$.

However, the observation of long-range magnetic orders in Ir^{5+} ($5d^4$) double perovskite oxides, such as Sr_2YIrO_6 and Ba_2YIrO_6, with reported μ_{eff} of 0.91 μ_B/Ir and 1.44 μ_B/Ir, respectively, raises questions regarding the ground state of these $5d^4$ oxides [183,184]. These findings have been met with challenges from other studies reporting the absence of magnetic order in Ba_2YIrO_6 [191] and Sr_2YIrO_6 [192] down to temperatures as low as ~430 mK. Investigations on A_2YIrO_6 (*A* = Sr, Ba) and other Ir^{5+} double perovskite oxides generally reveal weak paramagnetic behavior with small μ_{eff} values ranging from 0.19 μ_B/Ir to 0.63 μ_B/Ir (as indicated in Table 3.10). These values are significantly lower than the theoretical spin-only value of $\mu_{eff} = 2.83$ μ_B/Ir, highlighting the dominance of SOC in determining the ground state of these systems.

The origin of these finite magnetic moments in Ir^{5+} oxides remains uncertain. One proposed

explanation by Cao *et al*. is the quenching of the $J = 0$ state for Ir^{5+} due to distortion of the IrO_6 octahedra in Sr_2YIrO_6 [193]. However, this scenario fails to explain the observed paramagnetic moment in the cubic Ba_2YIrO_6, which lacks structural distortion. Studies on $Ba_{2-x}Sr_xYIrO_6$ have also found no correlation between the μ_{eff} values and the degree of structural distortions [194,195]. The presence of magnetic impurities has been suggested in studies on Sr_2YIrO_6 [192] and Ba_2YIrO_6 [196]. Fuchs *et al*. confirmed the existence of Ir^{4+} and Ir^{6+} magnetic defects, which are responsible for the magnetism observed in Ba_2YIrO_6 [197]. Antisite disorder in double perovskites has also been proposed to play a significant role [198,199]. Laguna-Marco *et al*. suggest that the Ir^{4+} and Ir^{6+} magnetic impurities may be located in regions of antisite disorder [199]. The condensation of $J = 1$ triplon excitations of $5d^4$ oxides is also considered as a possible source for the observed magnetic moments [193,194]. Chen *et al*. propose that the condensation is unlikely in Sr_2YIrO_6 and Ba_2YIrO_6 with ideal crystal structures, but the presence of antisite disorder between Y^{3+} and Ir^{5+} can break down local nonmagnetic singlets [198]. Recent studies on A_2BIrO_6 (A = Ba, Sr; B = Lu, Sc) also support the $J = 0$ ground state for these Ir^{5+} oxides and indicate that the magnetic signals arise from extrinsic sources, such as magnetic impurities and antisite disorder [200].

Table 3.10: Summary of space group (S.G.) and magnetic properties of Ir^{5+} oxides with double perovskite structures.

Material	S.G.	χ_0 (10^{-4} emu mol^{-1} Oe^{-1})	μ_{eff} (μ_B/Ir)	θ_{Weiss} (K)	Refs.
Ba_2YIrO_6	*Fm*-3*m*	-	0.3	-10	201
Ba_2YIrO_6	*Fm*-3*m*	4.8	0.63	-5	198
Ba_2YIrO_6	*Fm*-3*m*	5.4	0.52	-4	198
Ba_2YIrO_6	*Fm*-3*m*	5.4	0.50	-8	198
Ba_2YIrO_6	*Fm*-3*m*	5.83	0.44	-8.9	191
Ba_2YIrO_6	*Fm*-3*m*	-	0.31	-	196
Ba_2YIrO_6	*Fm*-3*m*	-	0.48	-16	197
Ba_2YIrO_6	*Fm*-3*m*	-3.9	1.44	-149	202
$Ba_{1.26}Sr_{0.74}YIrO_6$	*Fm*-3*m*	4.4	0.64	-18	202
$Ba_{2-x}Sr_xYIrO_6$	*Fm*-3*m*	-	0.47	-	194
Sr_2YIrO_6	$P2_1/n$	-	0.91	-229	193
Sr_2YIrO_6	$P2_1/n$	5.90	0.21	-2.8	192
Sr_2YIrO_6	$P2_1/n$	-	0.3	-	199
$Sr_{1.6}Ca_{0.4}YIrO_6$	$P2_1/n$	-	0.6	-	199
Sr_2LuIrO_6	$P2_1/n$	5.49	0.27	-2.55	200
Ba_2LuIrO_6	*Fm*-3*m*	4.98	0.42	-13.2	200
Sr_2ScIrO_6	$P2_1/n$	5.43	0.32	-10.7	200
Ba_2ScIrO_6	*Fm*-3*m*	5.10	0.48	-18.7	200
Bi_2NaIrO_6	$P2_1/n$	6.3	0.19	-6.8	203
$LaSrMgIrO_6$	$P2_1/n$	3.5	0.61	7	204
$LaSrZnIrO_6$	$P2_1/n$	3.9	0.46	1	204

3.2.4 $A_2BIr^{6+}O_6$ (A = Sr, Ba; B = Ca, Mg, Zn, Cu, Ni)

Ir^{6+} ($5d^3$) in an octahedral coordination typically requires high oxygen pressure or high-pressure conditions to stabilize in a perovskite structure (as shown in Table 3.11). This is likely the reason why there are fewer reported Ir^{6+}-based double perovskite oxides compared to their Ir^{5+} and Ir^{4+} counterparts. Double perovskite oxides, such as Sr_2BIrO_6 (B = Ca, Mg, Zn) [205,206], which contain a single Ir^{6+}-magnetic sublattice, exhibit AFM order. This observation is consistent with the behavior observed in double perovskites containing single Os^{5+}-magnetic sublattices, where all of them exhibit AFM ordering [207]. Comparing to double perovskites with a single Ir^{4+} magnetic sublattice (with ordering temperatures T_N = 7-12 K), Sr_2BIrO_6 (B = Ca, Mg, Zn) exhibit significantly higher magnetic ordering temperatures (T_N = 46-74 K). Despite the magnetic interactions occurring via the Ir-O-O-Ir pathway, the observed Weiss temperatures in Sr_2BIrO_6 (B = Ca, Mg, Zn) are relatively large (around -363 to -430 K), indicating a strong AFM coupling between Ir^{6+}-O-O-Ir^{6+}.

Double perovskite oxides containing both Ni^{2+} and Ir^{6+} ions have generated significant interest in the scientific community. According to the Goodenough-Kanamori rules, double perovskite oxides with d^8-d^3 electronic configurations are expected to exhibit FM behavior [182]. Consistent with this expectation, the d^8-d^3 double perovskite oxide La_2NiMnO_6 does indeed exhibit a FM ground state [208]. However, the compounds Sr_2NiIrO_6 and Ba_2NiIrO_6 display AFM ground states. In Sr_2NiIrO_6 and Ba_2NiIrO_6, there exist nearest neighbor Ni^{2+}–O–Ir^{6+} interactions, as well as next nearest neighbor Ni^{2+}–O–O–Ni^{2+} and Ir^{6+}–O–O–Ir^{6+} interactions. Theoretical calculations on Sr_2NiIrO_6 suggest that the next nearest neighbor Ir^{6+}–O–O–Ir^{6+} interactions are AFM and stronger than the next nearest FM Ni^{2+}–O–Ir^{6+} interactions, leading to an overall AFM ground state [209]. This explains the observed AFM behavior in Sr_2NiIrO_6 and Ba_2NiIrO_6, which is contrary to the simple expectation based on the Goodenough-Kanamori rules.

In contrast to Sr_2NiIrO_6, the AFM state of Ba_2NiIrO_6 is not as robust. Despite exhibiting AFM ordering at 51 K, the positive value of θ_{Weiss} indicates that FM interactions are dominant in Ba_2NiIrO_6. At low temperatures, when an external magnetic field is applied, Ba_2NiIrO_6 undergoes a field-induced spin-flop transition, transitioning from the AFM state to a state that is near FM [210]. This suggests that there is a strong competition between FM and AFM interactions in Ba_2NiIrO_6.

Table 3.11: Summary of space group (S.G.), synthetic pressure, and magnetic properties of Ir^{6+} oxides with double perovskite structures.

Material	S.G.	Synthetic pressure	Properties	T_{mag} (K)	μ_{eff} (μ_B/Ir)	θ_{Weiss} (K)	Refs.
Sr_2CaIrO_6	$P2_1/n$	20 MPa (O_2)	AFM	58	3.43	-363	205
Sr_2MgIrO_6	$P2_1/n$	20 MPa (O_2)	AFM	74	2.12	-418	205
Sr_2ZnIrO_6	$P2_1/n$	20 MPa (O_2)	AFM	46	3.82	-430	206
Ba_2CaIrO_6	Cubic	6 GPa	-				211
Ba_2SrIrO_6	Rhombohedral	60 MPa	-				211
Ba_2ZnIrO_6	Cubic	7 GPa	-				211
$BaLaLiIrO_6$	Cubic	7.5 GPa	-				211
Sr_2CuIrO_6	$I4/m$	4 GPa	AFM	15	4.24	-374	212
Sr_2NiIrO_6	$P2_1/n$	20 MPa (O_2)	AFM	58			206
Ba_2NiIrO_6	Fm-3m	8 GPa	AFM	51	4.67	80	210

4. Discussion and prospects

The $A_2BB'O_6$ double perovskite oxides constitute a vast family of compounds, facilitated by the inherent flexibility of the double perovskite structure. The presence of 5d electrons at the B' site has generated substantial interest, driven by the profound influence of relativistic effects.

The primary focus of this review paper is on three categories of 5d-electron oxides (Ir, Os, and Re) that crystallize into the rock-salt type double perovskite structure. With respect to synthesis of materials, high-pressure and high-temperature technique has demonstrated its effectiveness in broadening the compound family of $A_2BB'O_6$ (B' = Re, Os, and Ir) double perovskite oxides. On one hand, the elevated pressure conditions contribute to stabilizing rock-salt type double perovskite structures, even when the tolerance factor exceeds 1. Furthermore, it facilitates the incorporation of Mn^{2+} or Pb^{2+} into the A site of the double perovskite structure. A list of double perovskite oxides $A_2BB'O_6$, synthesized under high pressure, is provided in Table 2.1. The achievement of material preparation provides a solid foundation for delving deeper into the physical properties exhibited by double perovskite oxides involving 5d electrons. This section consolidates various experimentally observed properties of $A_2BB'O_6$ (B' = Re, Os, and Ir) double perovskite oxides and outlines the prospects into the following points.

(1) Remarkable high-temperature FIM compounds, characterized by exceptionally high Curie temperatures, have been found within the categories of Re-based and Os-based double perovskite oxides as tabulated in Table 4.1. The specific electronic configurations of Cr^{3+} ($3d^3$) and Fe^{3+} ($3d^5$) play pivotal roles in facilitating robust magnetic interactions, resulting in the emergence of high-T_C FIM within the $A_2BB'O_6$ (B = Cr, Fe; B' = Re, Os) double perovskite compounds.

In addition to their high-T_C FIM properties, Re-based and Os-based double perovskite oxides, demonstrate a diverse range of electron transport characteristics. The A_2FeReO_6 compound exhibits a range of electron transport behaviors, spanning from insulating to metal-insulator transitions and half-metallicity. Strikingly, Sr_2CrOsO_6 boasts the highest T_C among bulk double perovskite oxides, soaring up to 725 K. A comprehensive understanding of electron transport and magnetic mechanisms in Sr_2CrOsO_6 and its electronic analogues Sr_2CrMO_6 (M = Ta, W, Re) is crucial to unraveling the metal-insulator transition in Mott-insulating systems. Such understanding necessitates further exploration through both experimental and theoretical approaches.

Table 4.1: High-T_C ferrimagnetic double perovskite $A_2BB'O_6$ (B' = Re or Os).

Cr-Re double perovskite					
Compound	Ca_2CrReO_6	Sr_2CrReO_6			
T_C (K)	360	635			
Reference	63	13,62,63			
Fe-Re double perovskite					
Compound	Ca_2FeReO_6	Sr_2FeReO_6	Ba_2FeReO_6	Mn_2FeReO_6	Pb_2FeReO_6
T_C (K)	525	400	315	520	420
Reference	62-65	63,66	64,67,68	36,37	69
Cr-Os and Fe-Os double perovskite					
Compound	Ca_2CrOsO_6	Sr_2CrOsO_6	Ca_2FeOsO_6		
T_C (K)	490	725	320		
Reference	70	70	15,71		

(2) The magnetic properties and ordering temperatures of double perovskite oxides are significantly influenced by their crystal structures. The evolution of magnetism in osmate double

perovskite oxides, under the influence of structural changes and A-site elements, has been elucidated through a discussion of A_2BOsO_6 (A = Ca, Sr, Ba; B = Fe, Co, Ni). In these 3d-5d double perovskite oxides as shown in Table 4.2, the competition between the nearest neighbor B-O-Os AFM coupling and the long-range superexchange interaction of B-O-Os-O-B results in the complexity in their magnetic ground state. The bent B-O-Os bonds in monoclinic structure may suppress the long-range superexchange interaction, favoring the dominance of B-O-Os AFM coupling. This could explain why monoclinic Ca_2BOsO_6 (B = Fe, Co, Ni) exhibit ferrimagnetic properties, while tetragonal Sr_2BOsO_6 (B = Fe, Co, Ni) are antiferromagnetic. Additionally, the FM interaction also plays a role in the magnetism of Sr_2NiOsO_6, as evidenced by its positive θ_{Weiss}. The FM interaction is even more pronounced in the cubic double perovskite Ba_2NiOsO_6, as indicated by the increase in θ_{Weiss} from 27 K to 113 K. This robust FM interaction leads to FM ordering in Ba_2NiOsO_6 above 100 K. Ba_2NiOsO_6 stands out as a ferromagnetic insulator.

Table 4.2: The structure and physical properties of double perovskite A_2BOsO_6 (B = Fe, Co, Ni).

Fe-Os double perovskite			
Compound	Ca_2FeOsO_6	$SrCaFeOsO_6$	Sr_2FeOsO_6
S.G.	$P2_1/n$	$P2_1/n$ (100 K)	$I4/m$
Physical properties	Insulator, FIM	FIM	Insulator, AFM
T_{mag} (K)	320	210	140, 67
θ_{Weiss} (K)			+80 or +24
Reference	15,71	71	71,85,97
Co-Os double perovskite			
Compound	Ca_2CoOsO_6	Sr_2CoOsO_6	
S.G.	$P2_1/n$	$I4/m$	
Physical properties	Insulator, FIM	Insulator, AFM	
T_{mag} (K)	145	108, 70	
θ_{Weiss} (K)	+5	-51	
Reference	104	44,105	
Ni-Os double perovskite			
Compound	Ca_2NiOsO_6	Sr_2NiOsO_6	Ba_2NiOsO_6
S.G.	$P2_1/n$	$I4/m$	Fm-3m
Physical properties	Insulator, FIM	Insulator, AFM	Insulator, FM
T_{mag} (K)	175	50	100 and 32
θ_{Weiss} (K)		+27	+113
Reference	46,103	46	16

A clear correlation emerges between the magnetic ordering temperature and the degree of structural distortion in Ir-based double perovskite oxides. The relationship is demonstrated in compounds Ln_2NiIrO_6 (Ln = La, Pr, Nd, Sm-Gd) and Ln_2CoIrO_6, where enhanced structural distortions correspond to higher magnetic ordering temperatures, as illustrated in Fig. 3.8 and Table 3.9.

(3) The synthesis of double perovskites with Pb at the A-site is achievable through the application of high-pressure and high-temperature condition. Three osmate double perovskite Pb_2BOsO_6 (B = Co, Ni, Zn) has been reported. Intriguingly, the inversion symmetry breaking induced by AFM ordering is observed in metallic Pb_2CoOsO_6 and Pb_2NiOsO_6. Further investigation is required to elucidate the origin of the metallic properties observed in Pb_2BOsO_6 (B = Co, Ni, Zn).

These Pb_2BOsO_6 compounds provide an intriguing platform for exploring the concept of a ferroelectric metal, challenging the conventional notion that most ferroelectrics are insulators. Beyond theoretical considerations, the practical applications of polar metals are noteworthy, as they hold the potential for developing nano-scaled capacitors.

To comprehend the metallicity in Pb_2BOsO_6 (B = Co, Ni, Zn), exploring the influence of pressure on the physical properties of these compounds could offer further insights into their intrinsic nature. However, the incorporation of both 3d and 5d elements within the same system adds additional complexities when examining their behavior under pressure. This emphasizes the necessity for ongoing future investigations to elucidate these intricate phenomena.

(4) The increasing interest in cubic 5d double perovskite oxides, which incorporate non-magnetic elements at the B site, is triggered by the quest to explore multipolar magnetism— a promising candidate for advancing quantum magnets. The potential for multipolar magnetism in these compounds arises from their distinctive features, such as robust SOC, significant separation between magnetic octahedra, and cubic symmetry. A thorough exploration of the multipolar characteristics of 5d cubic double perovskite oxides is still ongoing and necessitates additional dedicated research efforts.

Table 4.3: Re-based and Os-based cubic double perovskite with potential for multipolar magnetism

Compound	Magnetism	T_{mag} (K)	θ_{Weiss} (K)	μ_{eff} (μ_B)	Ref.
Ba_2CdReO_6	Quadrupole order (25 K), canted AFM (12 K)	25, 12	-15.3	0.720	[137]
Ba_2NaOsO_6	Canted FM, quadrupolar order	~10			[123]
Ba_2CaOsO_6	Ferro-octupolar order	49			[121]
Ba_2MgOsO_6	Ferro-octupolar order	51			[121]
Ba_2ZnOsO_6	Ferro-octupolar order	30			[121]

The fundamental research on the bulk form of 5d double perovskite, encompassing synthesis, crystal structure, and physical properties, lays the groundwork for advancing potential applications within this category of materials. Due to the diverse magnetic and electrical features inherent in 5d double perovskite oxides, numerous promising applications are anticipated to emerge, including spintronic devices, nonvolatile data memory devices, electrocatalysts, magnetic field sensors, nano-scaled capacitors, and field-effect transistors. The FIM double perovskite with a high magnetic transition temperature shows promise for utilization in spintronic devices as electrodes within magnetic tunnel junctions (MTJ). This potential stems from its advantageous low-field tunneling magnetoresistance effect. The fabrication of MTJ devices based on double perovskite Sr_2FeMoO_6 has been reported [213-215]. However, further exploration of devices based on 5d double perovskites, exemplified by A_2FeReO_6, is still needed. FM or FIM insulators represent another category of materials with promising applications in spintronic devices. For instance, spin-filtering devices require FM or FIM insulators as tunnel barriers [216]. The rock-salt double perovskite Ba_2NiOsO_6 is identified as a FM insulator, while a range of FIM insulators has been extensively discovered in Re, Os, Ir-based double perovskite oxides. These compounds offer potential materials for the future development of spin-filtering devices. Additionally, Ir-based double perovskite oxides, such as Ba_2LnIrO_6 (Ln = Y, La, Ce, Pr, Nd, Tb), have been reported for their efficacy as highly active oxygen-evolving catalysts in acid media. Notably, these Ir-based double perovskite

oxides demonstrate a more cost-effective alternative compared to conventional catalyst IrO_2 [217].

In conclusion, the 5d transition metal oxides differ from their 3d or 4d by featuring more spatially extended 5d orbitals, resulting in relatively stronger hybridization with neighboring orbitals. Consequently, they possess a broader bandwidth and lower density of states near the Fermi level, leading to a reduction in electronic correlations. This unique characteristic of 5d transition metal elements, coupled with the inter-element spacing in the double perovskite structure, distinguishes 5d double perovskite oxides from their 3d counterparts. A notable example that highlights the disparity between 3d and 5d oxides is the analysis of magnetic properties using the Goodenough-Kanamori rules. La_2NiMnO_6, a $3d^8$-$3d^3$ double perovskite oxide, demonstrates a FM ground state in line with the expectations of Goodenough-Kanamori rules. Conversely, Sr_2NiIrO_6 and Ba_2NiIrO_6, featuring a $3d^8$-$5d^3$ configuration, exhibit an AFM ground state. In the solid solution $Sr_2Cr_{0.5}Ni_{0.5}OsO_6$, the FM exchange interaction of the $3d^8$-$5d^3$ configuration (Ni^{2+}-O-Os^{5+}) is more robust than that of the $3d^8$-$3d^3$ configuration (Ni^{2+}-O-Cr^{3+}). These findings collectively indicate the pivotal role of the 5d orbital in determining the competition of different virtual hopping routes. The question of how to deduce magnetic ground states from the classical Goodenough-Kanamori rules for 5d transition metal oxides remains intriguing and holds significance for the scientific community. In terms of practical applications, the 5d double perovskite oxides exhibit a wide range of physical properties, including high-T_C FIM, half-metallicity, high-T_C FIM, insulating FM, polar ferroelectrics, and multipolar magnetism. These properties hold great promise for spintronic device and advancing quantum materials.

Acknowledgment
J.C. thanks Professor J.-S Zhou for fruitful discussions. MANA is supported by the World Premier International Research Center Initiative (WPI) of MEXT, Japan. This research was partly funded by a Grant-in-Aid for Scientific Research from the Japan Society for the Promotion of Science (No. JP22H04601) and the Kazuchika Okura Memorial Foundation (No. 2022-11).

References

1. Li, L., and Yan, M., *Journal of Materials Science & Technology* (2023) **136**, 1
2. Zhang, Y.*, et al.*, *Acta Materialia* (2022) **226**, 117669
3. Xu, P.*, et al.*, *Materials Today Physics* (2021) **20**, 100470
4. Koskelo, E. C.*, et al.*, *Chemistry of Materials* (2022) **34** (7), 3440
5. Wu, B.*, et al.*, *Ceramics International* (2021) **47** (5), 6290
6. Li, L.*, et al.*, *Acta Materialia* (2020) **194**, 354
7. Hayashi, N.*, et al.*, *Angewandte Chemie International Edition* (2011) **50** (52), 12547
8. Jin, C.-Q.*, et al.*, *Proceedings of the National Academy of Sciences* (2008) **105** (20), 7115
9. Shi, Y.*, et al.*, *Journal of the American Chemical Society* (2013) **135** (44), 16507
10. Blaha, P.*, et al.*, *The Journal of Chemical Physics* (2020) **152** (7)
11. Longo, J., and Ward, R., *Journal of the American Chemical Society* (1961) **83** (13), 2816
12. Sleight, A. W.*, et al.*, *Inorganic Chemistry* (1962) **1** (2), 245
13. Fuoco, L.*, et al.*, *Chemistry of Materials* (2011) **23** (24), 5409
14. Feng, H. L.*, et al.*, *Journal of Solid State Chemistry* (2013) **201**, 186
15. Feng, H. L.*, et al.*, *Journal of the American Chemical Society* (2014) **136** (9), 3326
16. Feng, H. L.*, et al.*, *Physical Review B* (2016) **94** (23), 235158

17. Chen, J.*, et al.*, *Physical Review B* (2020) **102** (18), 184418
18. Princep, A. J.*, et al.*, *Physical Review B* (2020) **102** (10), 104410
19. Yamaura, K., *Journal of Solid State Chemistry* (2016) **236**, 45
20. Feng, H. L.*, et al.*, *Chemistry of Materials* (2017) **29** (2), 886
21. Kayser, P.*, et al.*, *Inorganic Chemistry* (2020) **59** (9), 6613
22. Li, M.-R.*, et al.*, *Angewandte Chemie International Edition* (2013) **52** (32), 8406
23. Cai, G.-H.*, et al.*, *Chemistry of Materials* (2017) **29** (13), 5447
24. King, G., and Woodward, P. M., *Journal of Materials Chemistry* (2010) **20** (28), 5785
25. Belik, A. A.*, et al.*, *Dalton Transactions* (2021) **50** (43), 15458
26. Yamada, I., *Science and Technology of Advanced Materials* (2017) **18** (1), 541
27. Woodward, P., *Acta Crystallographica Section B* (1997) **53** (1), 32
28. Howard, C. J.*, et al.*, *Acta Crystallographica Section B* (2003) **59** (4), 463
29. Goodenough, J.*, et al.*, High Pressure Synthesis. In *Preparative methods in solid state chemistry*, Academic Press, New York(1972)
30. Azuma, M.*, et al.*, 4.20 - High pressure studies of transition metal oxides. In *Comprehensive Inorganic Chemistry III (Third Edition)*, Reedijk, J., and Poeppelmeier, K. R., (eds.) Elsevier, Oxford, (2023), pp 681
31. Solana-Madruga, E.*, et al.*, *Journal of Materials Chemistry C* (2022) **10** (11), 4336
32. Frank, C. E.*, et al.*, *Chemical Communications* (2019) **55** (23), 3331
33. Solana-Madruga, E.*, et al.*, *Chemical Communications* (2020) **56** (83), 12574
34. Arévalo-López, A. M.*, et al.*, *Chemical Communications* (2016) **52** (32), 5558
35. Li, M.-R.*, et al.*, *Chemistry of Materials* (2016) **28** (9), 3148
36. Li, M.-R.*, et al.*, *Angewandte Chemie International Edition* (2015) **54** (41), 12069
37. Arévalo-López, A. M.*, et al.*, *Angewandte Chemie International Edition* (2015) **54** (41), 12074
38. Feng, H. L.*, et al.*, *Chemistry of Materials* (2021) **33** (11), 4188
39. Jacobsen, H.*, et al.*, *Physical Review B* (2020) **102** (21), 214409
40. Rammeh, N.*, et al.*, *physica status solidi c* (2006) **3** (9), 3225
41. da Cruz Pinha Barbosa, V.*, et al.*, *Chemistry of Materials* (2022) **34** (3), 1098
42. Feng, H. L.*, et al.*, *Journal of Solid State Chemistry* (2016) **243**, 119
43. Kermarrec, E.*, et al.*, *Physical Review B* (2015) **91** (7), 075133
44. Morrow, R.*, et al.*, *Journal of the American Chemical Society* (2013) **135** (50), 18824
45. Retuerto, M.*, et al.*, *European Journal of Inorganic Chemistry* (2008) **2008** (4), 588
46. Macquart, R.*, et al.*, *Inorganic Chemistry* (2005) **44** (26), 9676
47. Demazeau, G.*, et al.*, *高圧力の科学と技術* (1998) **7**, 1025
48. Tran, P. M.*, et al.*, *Journal of Solid State Chemistry* (2023) **317**, 123667
49. Feng, H. L.*, et al.*, *Physical Review Materials* (2020) **4** (6), 064420
50. Shi, Y.*, et al.*, *Nature Materials* (2013) **12** (11), 1024
51. Retuerto, M.*, et al.*, *Chemistry of Materials* (2015) **27** (12), 4450
52. Stoyanova-Lyubenova, T.*, et al.*, *Dalton Transactions* (2014) **43** (3), 1117
53. Yuan, Y.*, et al.*, *Inorganic Chemistry* (2015) **54** (7), 3422
54. Feng, H. L.*, et al.*, *Journal of Solid State Chemistry* (2014) **217**, 9
55. Feng, H. L.*, et al.*, *Physics Procedia* (2013) **45**, 117
56. Zhao, Q.*, et al.*, *Inorganic Chemistry* (2016) **55** (19), 9816
57. Vasala, S.*, et al.*, *Journal of Solid State Chemistry* (2014) **220**, 28
58. Feng, H. L.*, et al.*, *Inorganic Chemistry* (2021) **60** (2), 1241
59. Feng, H. L.*, et al.*, *Inorganic Chemistry* (2019) **58** (1), 397
60. Kobayashi, K. I.*, et al.*, *Nature* (1998) **395** (6703), 677
61. Wakabayashi, Y. K.*, et al.*, *Nature Communications* (2019) **10** (1), 535
62. Kato, H.*, et al.*, *Applied Physics Letters* (2002) **81** (2), 328

63. Kato, H.*, et al.*, *Physical Review B* (2004) **69** (18), 184412
64. Prellier, W.*, et al.*, *Journal of Physics: Condensed Matter* (2000) **12** (6), 965
65. Jeon, B. C.*, et al.*, *Journal of Physics: Condensed Matter* (2010) **22** (34), 345602
66. De Teresa, J. M.*, et al.*, *Applied Physics Letters* (2007) **90** (25), 252514
67. Ferreira, F. F.*, et al.*, *Journal of Synchrotron Radiation* (2006) **13** (1), 46
68. Azimonte, C.*, et al.*, *Physical Review Letters* (2007) **98** (1), 017204
69. Nishimura, K.*, et al.*, *Inorganic Chemistry* (2009) **48** (13), 5962
70. Morrow, R.*, et al.*, *Journal of Solid State Chemistry* (2016) **238**, 46
71. Morrow, R.*, et al.*, *Inorganic Chemistry* (2014) **53** (15), 7983
72. Kobayashi, K. I.*, et al.*, *Physical Review B* (1999) **59** (17), 11159
73. De Teresa, J. M.*, et al.*, *Journal of Magnetism and Magnetic Materials* (2005) **290-291**, 1043
74. Wu, H., *Physical Review B* (2001) **64** (12), 125126
75. Hauser, A. J.*, et al.*, *Physical Review B* (2012) **85** (16), 161201
76. Serrate, D.*, et al.*, *Journal of Physics: Condensed Matter* (2007) **19** (2), 023201
77. Gopalakrishnan, J.*, et al.*, *Physical Review B* (2000) **62** (14), 9538
78. Sriti, F.*, et al.*, *Journal of Magnetism and Magnetic Materials* (2002) **250**, 123
79. Herrero-Martín, J.*, et al.*, *Journal of Physics: Condensed Matter* (2005) **17** (33), 4963
80. Alonso, J. A.*, et al.*, *Chemistry of Materials* (2000) **12** (1), 161
81. De Teresa, J. M.*, et al.*, *Physical Review B* (2004) **69** (14), 144401
82. Iwasawa, H.*, et al.*, *Physical Review B* (2005) **71** (7), 075106
83. Granado, E.*, et al.*, *Physical Review B* (2019) **99** (19), 195118
84. Kato, H.*, et al.*, *Physical Review B* (2002) **65** (14), 144404
85. Paul, A. K.*, et al.*, *Inorganic Chemistry* (2013) **52** (11), 6713
86. Rodriguez, E. E.*, et al.*, *Physical Review Letters* (2011) **106** (6), 067201
87. Shi, Y. G.*, et al.*, *Physical Review B* (2009) **80** (16), 161104
88. Philipp, J. B.*, et al.*, *Physical Review B* (2003) **68** (14), 144431
89. Taylor, A. E.*, et al.*, *Physical Review B* (2015) **91** (10), 100406
90. Meetei, O. N.*, et al.*, *Physical Review Letters* (2013) **110** (8), 087203
91. Krockenberger, Y.*, et al.*, *Physical Review B* (2007) **75** (2), 020404
92. Jeng, H.-T., and Guo, G. Y., *Physical Review B* (2003) **67** (9), 094438
93. Vaitheeswaran, G.*, et al.*, *Applied Physics Letters* (2005) **86** (3), 032513
94. Vaitheeswaran, G.*, et al.*, *Journal of Physics: Conference Series* (2006) **29** (1), 50
95. Majewski, P.*, et al.*, *Applied Physics Letters* (2005) **87** (20), 202503
96. Majewski, P.*, et al.*, *Physical Review B* (2005) **72** (13), 132402
97. Feng, H. L.*, et al.*, *High Pressure Research* (2013) **33** (1), 221
98. Veiga, L. S. I.*, et al.*, *Physical Review B* (2015) **91** (23), 235135
99. Paul, A. K.*, et al.*, *Physical Review Letters* (2013) **111** (16), 167205
100. Bertaut, E. F.*, et al.*, *Journal of Applied Physics* (2004) **37** (3), 1038
101. Adler, P.*, et al.*, *Physical Review B* (2019) **99** (13), 134443
102. Haskel, D.*, et al.*, *Physical Review B* (2011) **84** (10), 100403
103. Morrow, R.*, et al.*, *Chemistry of Materials* (2016) **28** (11), 3666
104. Morrow, R.*, et al.*, *Physical Review B* (2015) **92** (9), 094435
105. Yan, B.*, et al.*, *Physical Review Letters* (2014) **112** (14), 147202
106. Paredes Aulestia, E. I.*, et al.*, *Applied Physics Letters* (2018) **113** (1), 012902
107. Gao, J. J.*, et al.*, *Physical Review B* (2020) **101** (22), 220101
108. Jiao, Y.*, et al.*, *Physical Review B* (2020) **102** (14), 144418
109. Azuma, M.*, et al.*, *Journal of the American Chemical Society* (2007) **129** (46), 14433
110. Bloch, D., *Journal of Physics and Chemistry of Solids* (1966) **27** (5), 881
111. Zhou, J. S., and Goodenough, J. B., *Physical Review Letters* (2002) **89** (8), 087201
112. Goodenough, J. B.*, et al.*, *Materials Research Bulletin* (1968) **3** (6), 471

113. Komarek, A. C.*, et al.*, *Physical Review Letters* (2008) **101** (16), 167204
114. Das, S.*, et al.*, *Physical Review B* (2020) **101** (18), 184422
115. Sakai, A., and Nakatsuji, S., *Journal of the Physical Society of Japan* (2011) **80** (6), 063701
116. Patri, A. S.*, et al.*, *Nature Communications* (2019) **10** (1), 4092
117. Fu, L., *Physical Review Letters* (2015) **115** (2), 026401
118. Harter, J. W.*, et al.*, *Science* (2017) **356** (6335), 295
119. Hayami, S.*, et al.*, *Physical Review B* (2018) **97** (2), 024414
120. Hirai, D.*, et al.*, *Physical Review Research* (2020) **2** (2), 022063
121. Maharaj, D. D.*, et al.*, *Physical Review Letters* (2020) **124** (8), 087206
122. Pourovskii, L. V.*, et al.*, *Physical Review Letters* (2021) **127** (23), 237201
123. Lu, L.*, et al.*, *Nature Communications* (2017) **8** (1), 14407
124. Liu, W.*, et al.*, *Physica B: Condensed Matter* (2018) **536**, 863
125. Chen, G.*, et al.*, *Physical Review B* (2010) **82** (17), 174440
126. Hirai, D., and Hiroi, Z., *Journal of the Physical Society of Japan* (2019) **88** (6), 064712
127. Morrow, R.*, et al.*, *Scientific Reports* (2016) **6** (1), 32462
128. Nilsen, G. J.*, et al.*, *Physical Review B* (2021) **103** (10), 104430
129. Fiore Mosca, D.*, et al.*, *Physical Review B* (2022) **106** (3), 035127
130. Churchill, D., and Kee, H.-Y., *Physical Review B* (2022) **105** (1), 014438
131. Rayyan, A.*, et al.*, *Physical Review B* (2023) **107** (2), L020408
132. Bharathy, M., and zur Loye, H. C., *Journal of Solid State Chemistry* (2008) **181** (10), 2789
133. Mogare, K. M.*, et al.*, *Journal of Solid State Chemistry* (2012) **191**, 153
134. Marjerrison, C. A.*, et al.*, *Inorganic Chemistry* (2016) **55** (20), 10701
135. Yamamura, K.*, et al.*, *Journal of Solid State Chemistry* (2006) **179** (3), 605
136. Ishikawa, H.*, et al.*, *Physical Review B* (2021) **104** (17), 174422
137. Hirai, D., and Hiroi, Z., *Journal of Physics: Condensed Matter* (2021) **33** (13), 135603
138. Stitzer, K. E.*, et al.*, *Solid State Sciences* (2002) **4** (3), 311
139. Steele, A. J.*, et al.*, *Physical Review B* (2011) **84** (14), 144416
140. Erickson, A. S.*, et al.*, *Physical Review Letters* (2007) **99** (1), 016404
141. Sasaki, Y.*, et al.*, *Journal of Materials Chemistry* (2002) **12** (8), 2361
142. Aharen, T.*, et al.*, *Physical Review B* (2010) **81** (6), 064436
143. Choy, J.-H.*, et al.*, *Solid State Ionics* (1998) **108** (1), 159
144. Thompson, C. M.*, et al.*, *Journal of Physics: Condensed Matter* (2014) **26** (30), 306003
145. Marjerrison, C. A.*, et al.*, *Physical Review B* (2016) **94** (13), 134429
146. Mikhailova, D.*, et al.*, *European Journal of Inorganic Chemistry* (2010) **2010** (8), 1196
147. Aczel, A. A.*, et al.*, *Physical Review B* (2016) **93** (21), 214407
148. Nishiyama, A.*, et al.*, *Journal of Solid State Chemistry* (2017) **248**, 134
149. Gao, H.*, et al.*, *Physical Review B* (2011) **83** (13), 134406
150. Ramesha, K.*, et al.*, *Chemistry of Materials* (2003) **15** (3), 668
151. Blasco, J.*, et al.*, *Dalton Transactions* (2011) **40** (13), 3211
152. Bramnik, K. G.*, et al.*, *Solid State Sciences* (2003) **5** (1), 235
153. Abakumov, A. M.*, et al.*, *Journal of Solid State Chemistry* (1997) **131** (2), 305
154. Cavichini, A. S.*, et al.*, *Physical Review B* (2018) **97** (5), 054431
155. Gao, S.*, et al.*, *Physical Review B* (2020) **101** (22), 220412
156. Greedan, J. E.*, et al.*, *Journal of Physics: Condensed Matter* (2011) **23** (16), 164213
157. Wiebe, C. R.*, et al.*, *Physical Review B* (2002) **65** (14), 144413
158. Popov, G.*, et al.*, *Physical Review B* (2003) **67** (2), 024406
159. Guerman, P.*, et al.*, *Journal of Physics: Condensed Matter* (2004) **16** (1), 135
160. Musa Saad H.-E, M., and Rammeh, N., *Solid State Communications* (2016) **248**, 129
161. Macquart, R. B.*, et al.*, *Journal of Solid State Chemistry* (2009) **182** (7), 1691
162. Corrêa, H. P. S.*, et al.*, *Cerâmica* (2010) **56**

163. Feng, H. L.*, et al.*, *Physical Review B* (2018) **97** (18), 184407
164. Russell, D. D.*, et al.*, *Inorganic Chemistry* (2016) **55** (5), 2240
165. Paul, A. K.*, et al.*, *Zeitschrift für anorganische und allgemeine Chemie* (2015) **641** (2), 197
166. Wakeshima, M.*, et al.*, *Journal of Solid State Chemistry* (2013) **197**, 236
167. Hinatsu, Y.*, et al.*, *Journal of Solid State Chemistry* (2013) **206**, 300
168. Gemmill, W. R.*, et al.*, *Journal of Solid State Chemistry* (2006) **179** (6), 1750
169. Gemmill, W. R.*, et al.*, *Inorganic Chemistry* (2005) **44** (8), 2639
170. Lufaso, M. W.*, et al.*, *Journal of Solid State Chemistry* (2008) **181** (3), 623
171. Feng, H. L.*, et al.*, Crystal Structure and Magnetic Properties of Sr_2LiOsO_6. In *Proceedings of the 12th Asia Pacific Physics Conference (APPC12)*, J. Phys. Soc. Jpn(2014), Vol. 1
172. Thakur, G. S.*, et al.*, *European Journal of Inorganic Chemistry* (2020) **2020** (42), 3991
173. Powell, A. V.*, et al.*, *Journal of Alloys and Compounds* (1993) **201**, 73
174. Cao, G.*, et al.*, *Phys. Rev. B* (2013) **87**, 155136
175. Jackeli, G., and Avella, A., *Phys. Rev. B* (2015) **92**, 184416
176. Catuneanu, A.*, et al.*, *Phys. Rev. B* (2015) **92**, 165108
177. Aczel, A. A.*, et al.*, *Phys. Rev. B* (2016) **93**, 214426
178. Aczel, A. A.*, et al.*, *Phys. Rev. B* (2019) **99**, 134417
179. Vogl, M.*, et al.*, *Phys. Rev. Mater.* (2020) **4**, 054413
180. Mugavero Iii, S. J.*, et al.*, *Journal of Solid State Chemistry* (2010) **183** (2), 465
181. Currie, R. C.*, et al.*, *J. Solid State Chem.* (1995) **116**, 199
182. Goodenough, J. B., *Magnetism and the chemical Bond*. Interscience, New York: 1963
183. Ferreira, T.*, et al.*, *Phys. Rev. Mater.* (2021) **5**, 064408
184. Kolchinskaya, K.*, et al.*, *Phys. Rev. B* (2012) **85**, 224422
185. Morrow, R.*, et al.*, *Inorg. Chem.* (2014) **53**, 7983
186. Hou, Y. S.*, et al.*, *Sci. Rep.* (2015) **5**, 13159
187. Morrow, R.*, et al.*, *Chem. Mater.* (2016) **28**, 3666
188. Ding, X.*, et al.*, *Phys. Rev. B* (2019) **99**, 014438
189. Feng, H. L.*, et al.*, *Inorg Chem* (2019) **58** (1), 397
190. Kim, B. J.*, et al.*, *Phys. Rev. Lett.* (2008) **101**, 076402
191. Dey, T.*, et al.*, *Phys. Rev. B* (2016) **93**, 014434
192. Corredor, L. T.*, et al.*, *Phys. Rev. B* (2017) **95**, 064418
193. Cao, G.*, et al.*, *Phys. Rev. Lett.* (2014) **112**, 056402
194. Phelan, B. F.*, et al.*, *Solid State Communications* (2016) **236**, 37
195. Ranjbar, B.*, et al.*, *Inorg. Chem.* (2015) **54**, 10468
196. Hammerath, F.*, et al.*, *Phys. Rev. B* (2017) **96**, 165108
197. Fuchs, S.*, et al.*, *Phys. Rev. Lett.* (2018) **120**, 237204
198. Chen, Q.*, et al.*, *Phys. Rev. B* (2017) **96**, 144423
199. Laguna-Marco, M. A.*, et al.*, *Phys. Rev. B* (2020) **101**, 014449
200. Aczel, A. A.*, et al.*, *Phys. Rev. Mater.* (2022) **6**, 094409
201. Nag, A.*, et al.*, *Phys. Rev. B* (2018) **98**, 014431
202. Terzic, J.*, et al.*, *Phys. Rev. B* (2017) **96**, 064436
203. Prasad, B. E.*, et al.*, *Chem. Eur. J.* (2018) **24**, 16762
204. Wolff, K. K.*, et al.*, *Z. Anorg. Allg. Chem.* (2017) **643**, 2095
205. Kayser, P.*, et al.*, *Eur. J. Inorg. Chem.* (2014) **2014**, 178
206. Kayser, P.*, et al.*, *Inorg. Chem.* (2013) **52**, 11013
207. Feng, H. L.*, et al.*, *J. Solid State Chem.* (2016) **243**, 119
208. Rogado, N. S.*, et al.*, *Adv. Mater.* (2005) **17**, 2225
209. Ou, X.*, et al.*, *Scientific Reports* (2014) **4**, 7542
210. Feng, H. L.*, et al.*, *Inorg. Chem.* (2021) **60**, 1241
211. Demazeau, G., *Journal of the Korean Chemical Society* (1998) **42**, 135

212. Vasala, S.*, et al.*, *J. Solid State Chem.* (2014) **220**, 28
213. Bibes, M.*, et al.*, *Applied Physics Letters* (2003) **83** (13), 2629
214. Asano, H.*, et al.*, *IEEE Transactions on Magnetics* (2005) **41** (10), 2811
215. Kumar, N.*, et al.*, *Journal of Physics D: Applied Physics* (2014) **47** (6), 065006
216. Bibes, M.*, et al.*, *Advances in Physics* (2011) **60** (1), 5
217. Diaz-Morales, O.*, et al.*, *Nature Communications* (2016) **7** (1), 12363